Marko S. Milosavljevic 📵 ; Rigo A. Carrasco 📵 ; Alexander T. Newell 👨 ; Jaden R. Love 📵 ; Stefan Zollner 📵 ; Christian P. Morath (b); Diana Maestas; Preston T. Webster (c); Shane R. Johnson (c)



J. Appl. Phys. 138, 093103 (2025) https://doi.org/10.1063/5.0285129

A CHORUS





# Articles You May Be Interested In

Measurement of InAsSb bandgap energy and InAs/InAsSb band edge positions using spectroscopic ellipsometry and photoluminescence spectroscopy

J. Appl. Phys. (December 2015)

Optical properties of InAsBi and optimal designs of lattice-matched and strain-balanced III-V semiconductor superlattices

J. Appl. Phys. (June 2016)

Impact of unintentional Sb in the tensile InAs layer of strain-balanced type-II InAs/InAsSb superlattices grown on GaSb by molecular beam epitaxy

J. Appl. Phys. (August 2023)











Unlock the Full Spectrum.





From DC to 8.5 GHz. Your Application. Measured.







# Spectroscopic ellipsometry measurement and analysis of the optical constants of InAs/InAsSb and InGaAs/InAsSb superlattices and their bulk constituents

Cite as: J. Appl. Phys. 138, 093103 (2025); doi: 10.1063/5.0285129 Submitted: 12 June 2025 · Accepted: 9 August 2025 · Published Online: 2 September 2025







Marko S. Milosavljevic, 1,2,3 D Rigo A. Carrasco, D Alexander T. Newell, D Jaden R. Love, D Stefan Zollner, D Christian P. Morath, 2 Diana Maestas, 2 Preston T. Webster, 2 and Shane R. Johnson 1, a) D

### **AFFILIATIONS**

- <sup>1</sup>Center for Photonics Innovation & Electrical, Computer, and Energy Engineering, Arizona State University, Tempe, Arizona 85287, USA
- <sup>2</sup>Air Force Research Laboratory, Space Vehicles Directorate, Kirtland Air Force Base, Albuguerque, New Mexico 87117, USA
- <sup>3</sup>A-Tech, LLC, a BlueHalo company (ATA BlueHalo), Albuquerque, New Mexico 87123, USA

ABSTRACT

The optical constants of strain-balanced InAs/InAsSb and InGaAs/InAsSb superlattices and their constituents GaAs, GaSb, InAs, InSb, and InAsSb are measured using spectroscopic ellipsometry. An optical constant model is developed that accurately describes the index of shape of the absorption coefficient in the vicinity of the fundamental bandgap of these III–V materials. The model of refraction in the vicinity of the bandgap energy, below-bandgap Urbach absorption in the vicinity of the bandgap is described using the optical structure model that comprises the light from the comprises the light from the comprises the comprises the comprises the light from the comprises the comprise the c light from the sample surface. The optical constant model is implemented within the optical structure model and fit to the measured ellipsometric data with the optical constants of the layer of interest as best-fit parameters. The superlattice measurements exhibit spurious periodic peaks in the optical constants extracted using the point-by-point fit method. Multi-sample analysis of identical midwave superlattices grown at different thicknesses significantly reduces the presence of the spurious peaks and, in general, improves the optical constant fit and the extraction of the absorption edge parameters. In comparing superlattice results, the InGaAs/InAsSb superlattices have a shorter period, demonstrate stronger absorption due to greater electron-hole wavefunction overlap, and exhibit broader absorption tails as a result of greater alloy and interface disorder.

© 2025 Author(s). All article content, except where otherwise noted, is licensed under a Creative Commons Attribution-NonCommercial-NoDerivs 4.0 International (CC BY-NC-ND) license (https://creativecommons.org/licenses/by-nc-nd/4.0/). https://doi.org/10.1063/5.0285129

# I. INTRODUCTION

The III-V arsenide and antimonide material systems grown on commercially available InAs and GaSb substrates offer high-quality pseudomorphic photodetectors for the technologically important midwave  $(3-5 \mu m)$  and longwave  $(8-12 \mu m)$  transparent atmospheric windows. 1-4 Bulk III-V alloys and type-II InAs/InAsSb superlattices

provide photodetector materials with long lifetimes and bandgap tunability<sup>5-9</sup> that make them viable for this design space. Nevertheless, pushing detection to longer wavelength cutoffs presents challenges for these material systems. For bulk alloys, this challenge is manifested in integrating multiple elements while maintaining smooth surface morphology during growth. 10,11 For type-II InAs/InAsSb superlattices,

Department of Physics, New Mexico State University, P.O. Box 30001, Las Cruces, New Mexico 88003, USA

the challenge lies in optimizing design to improve absorption and vertical transport properties by maximizing electron–hole wavefunction overlap and improving heavy-hole mobility. 12–14

Incorporating Ga into the superlattice tensile layer to form InGaAs/InAsSb superlattices<sup>14,15</sup> is utilized as a method to improve performance. This approach enables a larger tensile strain that facilitates more symmetric layer thicknesses in the strain-balance between the tensile and compressive layers. The resulting performance benefits include decreasing the necessary superlattice period to achieve a certain cutoff wavelength, increasing electron-hole wavefunction overlap, and reducing heavy-hole confinement. Nevertheless, introducing Ga increases the chemical inhomogeneity of the superlattice. Quantifying the impact of these effects is, therefore, important in realizing the performance tradeoffs in these materials for photodetection.

To this end, the optical constants of these materials are investigated and analyzed to provide a comparison of their absorption properties and subsequent performance as photodetectors. Specifically, the width of the absorption edge is impacted by the presence of frozen-in tail states <sup>16–19</sup> that result from alloy disorder in bulk materials and both alloy and interface disorder in superlattices. Furthermore, the magnitude and spectral shape of the absorption coefficient near the fundamental bandgap is impacted by the electron–hole wavefunction overlap, <sup>20</sup> the electron–hole Coulomb interaction, <sup>21–25</sup> and the presence of tail states. <sup>16,18</sup>

An optical constant model is developed as a method of analysis for the materials investigated, where the significant model parameters are based on physical features observed in experimental measurements of the fundamental absorption edge. These consist of the Urbach energy that describes the characteristic width of the sub-gap exponential absorption edge <sup>16,18,21,26</sup> that transitions to a power law at energies above the bandgap. The model does not describe exciton absorption as its characteristic features are not observed in the materials investigated. The measurements are at room temperature where excitons readily dissociate as their binding energy is small compared to the thermal energy. <sup>28–30</sup> Consequently, the contribution of excitons to the optical-absorption spectrum is significantly diminished or absent. <sup>27,31</sup>

Various optical constant models have been developed and presented in the literature<sup>23–25,32</sup> that describe the fundamental absorption edge in III-V and other semiconductor materials. The initial work<sup>23,24</sup> established the role of the joint optical density of states and the Coulomb interaction in shaping absorption spectra near the band edge. Building on these principles, analytical expressions for the optical constants of III-V materials were developed that incorporate empirical broadening terms to account for subbandgap absorption features.<sup>25,32</sup> The description of absorption tails has since evolved, with theoretical foundations for the subbandgap Urbach tail established by linking it to disorder-induced band tail states. 16,18 While these models are grounded in solid-state physics and contribute to the understanding of optical transitions, they do not seamlessly describe a broad range of materials, and hence are not suitable for the analysis in this work. Alternatively, models such as PSEMI<sup>33</sup> are widely used in the Woollam analysis software<sup>34</sup> and are highly flexible and suitable for a wide range of materials, but at the expense of physical interpretability. Furthermore, they do not accurately replicate the sharp exponential

Urbach tails observed in some materials investigated. In this work, an absorption edge model<sup>21</sup> is further developed to specifically describe the index of refraction in the vicinity of the bandgap using Kramers–Kronig integration over the absorption edge.

In this work, the optical constants of InAs/InAsSb and InGaAs/InAsSb superlattices and their constituent binaries GaAs, GaSb, InAs, and InSb, and ternary alloy InAsSb are investigated using spectroscopic ellipsometry (SE). The theoretical approach and the optical constant model are presented in Sec. II. The sample properties and structural characterization are presented in Sec. III. The spectroscopic ellipsometry measurements, modeling, and determination of optical constants are presented in Secs. IV and V. The analysis and interpretation of the results are presented in Secs. VI and VII.

#### II. THEORY AND OPTICAL CONSTANTS MODEL

In general, spectroscopic ellipsometry measures the amplitude ratio and phase difference of p- and s-polarized light<sup>35</sup> reflected from the surface of a structure, which is described as

$$\frac{R_p}{R_s} = \tan{(\Psi)}e^{i\Delta}.$$
 (1)

Here, the complex Fresnel reflection coefficients are  $R_p$  for p-polarized light (parallel to the plane of incidence) and  $R_s$  for s-polarized light (perpendicular to the plane of incidence). Furthermore, their complex ratio is typically expressed in terms of the ellipsometric angles  $\Psi$  and  $\Delta$ , where  $\tan{(\Psi)}$  is the amplitude ratio and  $\Delta$  is the phase difference.

The reflection and transmission of a plane wave from a single film on a semi-infinite thick substrate, described in terms of ray optics, is illustrated in Fig. 1 for the typical case where the measurements are performed in ambient conditions. The optical, physical, and ray parameters are indicated for each layer, where N = n - ik

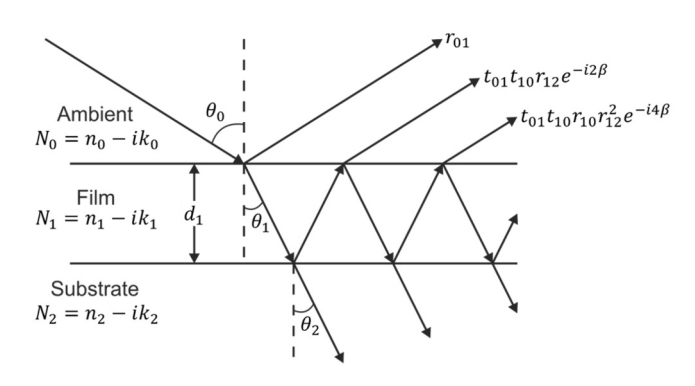


**FIG. 1.** Reflection and transmission of a plane wave shown by arrows that originates in the ambient for a thin film on a substrate with parallel-plane boundaries. The numerical subscript for each layer medium is 0 for the ambient, 1 for the film, and 2 for the substrate. Here, d designates the layer thickness, N=n-ik is the complex index of refraction, and  $\theta$  is the complex angle of propagation with respect to the surface normal. In this case, the film thickness is  $d_1$  and the ambient and substrate thicknesses are assumed to be semi-infinite.

is the complex index of refraction, d is the layer thickness, and  $\theta$  is the complex angle of propagation with respect to the surface normal. The parameter subscripts denote which property belongs to a particular layer medium with 0 for the ambient, 1 for the thin film of interest, and 2 for the substrate.

When the incident wave reaches the ambient-film interface, a fraction of the wave intensity reflects back into the ambient while the remainder transmits into the film. The complex Fresnel interface coefficients are r for reflection and t for transmission of p- and s-polarized light<sup>35</sup> with

$$r_{01p} = \frac{N_1 \cos(\theta_0) - N_0 \cos(\theta_1)}{N_1 \cos(\theta_0) + N_0 \cos(\theta_1)},$$
 (2a)

$$r_{01s} = \frac{N_0 \cos(\theta_0) - N_1 \cos(\theta_1)}{N_0 \cos(\theta_0) + N_1 \cos(\theta_1)},$$
 (2b)

$$t_{01p} = \frac{N_0}{N_1}(r_{01p} + 1) = \frac{2N_0\cos(\theta_0)}{N_1\cos(\theta_0) + N_0\cos(\theta_1)},$$
 (2c)

$$t_{01s} = r_{01s} + 1 = \frac{2N_0 \cos(\theta_0)}{N_0 \cos(\theta_0) + N_1 \cos(\theta_1)}$$
, (2d)

where the subscript 01 denotes the interface between layers 0 and 1, and subscripts p and s denote p- or s- polarized light. The angle of incidence  $\theta_0$  and the index of refraction  $N_0 \cong 1$  are presupposed to be real as the ambient atmosphere is assumed to be transparent, with  $k/n < 10^{-5}$ , which is valid for most infrared wavelengths examined in this work. Exceptions may occur at strong infrared absorption lines centered at  $6.2 \,\mu m$  and  $4.3 \,\mu m$  (200 meV and 290 meV) due to low concentrations of H2O and CO2 gas in the ambient, respectively. The angles of refraction  $\theta_1$  and  $\theta_2$ and indices of refraction  $N_1$  and  $N_2$  are complex and are related angle of incidence via Snell's  $N_0 \sin(\theta_0) = N_1 \sin(\theta_1) = N_2 \sin(\theta_2)$ . The complex Fresnel reflection coefficient of the entire structure is determined by summing all contributions of the partial plane wave in the ambient as<sup>3</sup>

$$R_{p} = r_{01p} + t_{01p}t_{10p}r_{12p}e^{-i2\beta} + t_{01p}t_{10p}r_{10p}r_{12p}^{2}e^{-i4\beta}$$

$$+ t_{01p}t_{10p}r_{10p}^{2}r_{12p}^{3}e^{-i6\beta} + \dots$$

$$= r_{01p} + \frac{t_{01p}t_{10p}r_{12p}e^{-i2\beta}}{1 - r_{10p}r_{12p}e^{-i2\beta}} = \frac{r_{01p} + r_{12p}e^{-i2\beta}}{1 + r_{10p}r_{12p}e^{-i2\beta}}, \qquad (2e)$$

$$R_s = \frac{r_{01s} + r_{12s}e^{-i2\beta}}{1 + r_{10s}r_{12s}e^{-i2\beta}},$$
 (2f)

where  $r_{10}=-r_{01}$ ,  $t_{01}t_{10}=1-r_{01}^2$ ,  $\beta=2\pi d_1N_1\cos(\theta_1)/\lambda$ , and  $\lambda=hc/hv$ , where  $\lambda$  and hv are the wavelength and photon energy of light, respectively; h is Planck's constant; and c is the speed of light. The dimensionless phase thickness  $\beta$  is inversely proportional to wavelength and is the phase change a wave experiences as it travels through the film from one interface to the next.

Last, the ellipsometric angles  $\Psi$  and  $\Delta$  are determined as

$$\Psi = \tan^{-1} \left( \frac{|R_p|}{|R_s|} \right), \tag{3a}$$

$$\Delta = \arg(R_p) - \arg(R_s),\tag{3b}$$

where arg() returns the argument (angle) of a complex number. For the simple case of a single film on a substrate, the Fresnel equations and ellipsometric angle equations in Eqs. (2) and (3) constitute an optical structure model that mathematically describes the reflection and transmission properties of the structure. The ellipsometric angles' output from the optical structure model,  $\Psi^{mod}$  and  $\Delta^{\text{mod}}$ , are fit to the experimentally measured ellipsometric angles  $\Psi^{exp}$  and  $\Delta^{exp}$  to determine the film thickness and the optical constants of the film, provided the optical constants of the substrate are known and vice versa.

For more general structures containing multiple homogeneous films with parallel interfaces, the total reflected amplitude of the structure can be determined using 2 x 2 transfer matrices. Specifically, a series of interface and layer matrices are defined that transfer the reflection and transmission effects of each interface and layer to the next within the structure. The interface matrix I is defined for p- and s-polarized light as

$$I_{(j-1)jp} = \frac{1}{t_{(j-1)jp}} \begin{bmatrix} 1 & r_{(j-1)jp} \\ r_{(j-1)jp} & 1 \end{bmatrix}, \tag{4a}$$

$$I_{(j-1)js} = \frac{1}{t_{(j-1)js}} \begin{bmatrix} 1 & r_{(j-1)js} \\ r_{(j-1)js} & 1 \end{bmatrix}, \tag{4b}$$

where the subscript j refers to the jth layer in the structure and  $r_{(j-1)j}$  and  $t_{(j-1)j}$  are the complex Fresnel coefficients for reflection and transmission at the interface of the j-1th and jth layers, g0 respectively. The layer matrix L is defined as g15

$$\mathbf{L}_{j} = \begin{bmatrix} e^{i\beta_{j}} & 0\\ 0 & e^{-i\beta_{j}} \end{bmatrix}, \tag{5}$$

where  $\beta_i = 2\pi d_i N_i \cos(\theta_i)/\lambda$  is the dimensionless phase thickness of the *i*th layer. The overall reflection and transmission properties of the structure are contained in the scattering matrix S that is defined separately for p- and s- polarized light as the product of the interface and layer matrices in the order given as

$$S_{p} = I_{01p} L_{1} I_{12p} L_{2} \dots I_{(j-1)jp} L_{j} \dots L_{m} I_{m(m+1)p}$$

$$= \begin{bmatrix} S_{11p} & S_{12p} \\ S_{21p} & S_{22p} \end{bmatrix}, \qquad (6a)$$

$$S_{s} = I_{01s}L_{1}I_{12s}L_{2}\dots I_{(j-1)js}L_{j}\dots L_{m}I_{m(m+1)s}$$

$$= \begin{bmatrix} S_{11s} & S_{12s} \\ S_{21s} & S_{22s} \end{bmatrix}, \qquad (6b)$$

where m is the number of layers between the ambient and the substrate and (m + 1) denotes the substrate. The reflected amplitudes from the structure specified by the p- and s-polarized Fresnel reflection coefficients  $R_p$  and  $R_s$  are determined by the ratios<sup>35</sup>

$$R_p = S_{21p}/S_{11p}, (7a)$$

$$R_s = S_{21s}/S_{11s}.$$
 (7b)

The Fresnel equations, ellipsometric angle equations, and transfer matrices in Eqs. (2)–(7) along with the sample layer structure constitute an optical structure model that is used to simulate the sample ellipsometric angles  $\Psi^{\rm mod}$  and  $\Delta^{\rm mod}$  that are fit to the experimentally measured angles  $\Psi^{\rm exp}$  and  $\Delta^{\rm exp}$ . In this type of analysis, the optical constants are usually expressed as either the complex dielectric function or the complex index of refraction, as shown in Fig. 1 and Eq. (2). The optical constants can be determined for one layer of the optical structure, provided they are known for all other layers. In the model, the complex index of refraction described as N=n-ik has real and imaginary components that are referred to as the index of refraction n(hv) and the extinction coefficient k(hv). For device work, it is desirable to work with the absorption coefficient  $\alpha(hv)$  that is related to the extinction coefficient via<sup>35</sup>

$$\alpha(hv) = k(hv) \left(\frac{4\pi hv}{hc}\right). \tag{8}$$

In which case, the index of refraction is related to the absorption coefficient via the Kramers–Kronig relation<sup>36</sup> with

$$n(hv) = 1 + \frac{hc}{2\pi^2} P \int_0^\infty \frac{\alpha(hv')}{hv'^2 - hv^2} dhv', \qquad (9)$$

where P denotes the Cauchy principal value of the integral.

In this work, an optical constant model is developed that describes the index of refraction and absorption coefficient in the vicinity of the fundamental band edge of direct bandgap semiconductor materials. The model encompasses (i) the widely observed exponential Urbach absorption edge  $^{18,26}$  tail below the bandgap, (ii) the observed power law dependence of the absorption coefficient above the bandgap, and (iii) a Kramers–Kronig consistent replication of the absorption edge  $\alpha(hv)$  in the spectral dependence of the index of refraction n(hv). The optical constant model is

$$\alpha(h\nu) = \alpha_g \left[ \frac{\ln\left(1 + e^{(h\nu - E_g)/(p(h\nu)E_u)}\right)}{\ln(2)} \right]^{p(h\nu)}, \quad (10a)$$

$$p(hv) = p_g + a_m(hv/E_g - 1)$$
, (10b)

$$n(hv) = n_0 + \frac{n_1}{1 - (hv/E_{\text{TO}})^2} + \frac{hc}{2\pi^2} P \int_0^{E_s} \frac{\alpha(hv')}{hv'^2 - hv^2} dhv'. \quad (10c)$$

Here,  $E_g$  is the bandgap energy,  $\alpha_g$  is the absorption coefficient at the bandgap,  $E_u$  is the Urbach energy<sup>18,21</sup> that describes the characteristic slope energy of the exponential absorption edge,  $p_g$ 

describes the power law relation observed in the absorption spectrum near the bandgap, and  $a_m$  describes the change in the power law p(hv) at energies above the bandgap as the Coulomb interaction weakens.<sup>21</sup>

The bandgap energy  $E_g$  depicts the boundary between the below-bandgap tail state transitions and the above-bandgap continuum state transitions. The textbook description of bandgap energy designates the bandgap as the sharp energy-cutoff in the optical transitions that occur at the valence and conduction continuum band edges. However, the ever-presence of tail states  $^{18,19}$  obscures the sharp cutoff in optical transitions involving the continuum states. In the absorption edge model, the above-bandgap  $hv \geq E_g$  absorption is described by the power law asymptote

$$\alpha_{+}(h\nu \ge E_g) = \alpha_g \left(\frac{h\nu - E_g}{\ln(2)p(h\nu)E_u}\right)^{p(h\nu)},\tag{10d}$$

and the below-bandgap  $hv \leq E_g$  absorption is described by the Urbach edge asymptote

$$\alpha_{-}(hv \le E_g) = \frac{\alpha_g}{(\ln(2))^{p(hv)}} e^{(hv - E_g)/E_u}$$

$$\cong \frac{\alpha_g}{(\ln(2))^{p_g}} e^{(hv - E_g)/E_u} . \tag{10e}$$

The index of refraction [Eq. (10c)] is described by a constant offset  $n_0$  that accounts for contributions to the index of refraction outside the measured range, a Sellmeier oscillator<sup>37</sup> that accounts for the influence of long-wavelength optical-absorption, and the Kramers-Kronig contribution of the fundamental Urbach absorp-Kramers-Kronig contribution of the fundamental Urbach absorption edge to the index of refraction in the vicinity of the bandgap. The Sellmeier oscillator describes the dispersion in the index of  $\frac{1}{2}$ refraction due to the strong absorption of the transverse optical (TO) phonon at energy  $E_{TO}$  with amplitude  $n_1$ . The integration over the absorption coefficient [Eqs. (10a) and (10b)] is terminated at photon energy  $E_s$  that is well above the bandgap. This term accounts for contributions to the offset and slope of the index of refraction near and above the bandgap that originate from absorption well above the bandgap. The constant offset in the index of refraction increases as the upper integration cutoff  $E_s$  increases, thus linking  $E_s$  with the offset  $n_0$ . It is, therefore, the observed slope of the index of refraction near and above the bandgap energies that determines the appropriate value of the integration cutoff  $E_s$ .

For the materials investigated, the optical constant model presented in Eqs. (10a)–(10c) yields equivalent numerical results to those given by a strict Kramers–Kronig consistent formulation. To enforce a Kramers–Kronig consistent form, the following steps are taken. (i) Causality dictates that Eq. (10c) be integrated from 0 to infinity,<sup>38</sup> which is achieved by defining the absorption coefficient as zero outside the photon energy range of interest ( $hv > E_s$ ). (ii) The absorption coefficient in Eqs. (10a) and (10b) is redefined as  $\alpha_{\rm odd}(hv) = \alpha(hv) - \alpha(-hv)$  to satisfy the odd parity requirement for causality and the application of the Kramers–Kronig relations,<sup>38</sup> which produces identical results to the original model, with the additional term,  $\alpha(-hv)$ , evaluating to zero within 16 digits of precision. (iii) The Sellmeier oscillator<sup>37</sup> term in Eq. (10c) technically

requires a Dirac delta function,  $\pi n_1 E_{TO} \delta(hv - E_{TO})/2$ , in the absorption coefficient at the TO phonon energy. However, since the TO phonon lies outside the experimental spectral range for the materials examined using a Sellmeier oscillator, omitting this term does not affect the fit or the values of the extracted parameters. Since these analytical refinements do not influence the numerical outcomes, the model in its current form provides Kramers-Kronig consistent results.

The model described in Eq. (10) provides a smooth, nineparameter model that yields Kramers-Kronig consistent optical constants in terms of the index of refraction and absorption coefficient and, for clarity, is referred to as the optical constant absorption edge model. This model provides a description of the impact of tail states on the absorption edge cutoff in terms of the bandgap energy and the Urbach energy. The implementation of a smooth parametrized optical constant model also allows the layer thickness for one or any number of the layers in the optical structure model to be determined in the fit analysis.

The connection between the absorption edge and the peak in the index of refraction is illustrated in Fig. 2, where n(hv) and  $\alpha(hv)$  are simulated using the optical properties of GaAs except that the width (Urbach energy) of the absorption edge is varied. The index of refraction on the left vertical axis and the absorption coefficient on the right vertical axis are shown as a function of photon energy with Urbach energies  $E_u$  that are 1 meV (black), 3 meV (blue), 10 meV (red), and 30 meV (green). The abovebandgap asymptote [Eq. (10d)] of the absorption coefficient is fixed, while the below-bandgap slope of the Urbach tail asymptote

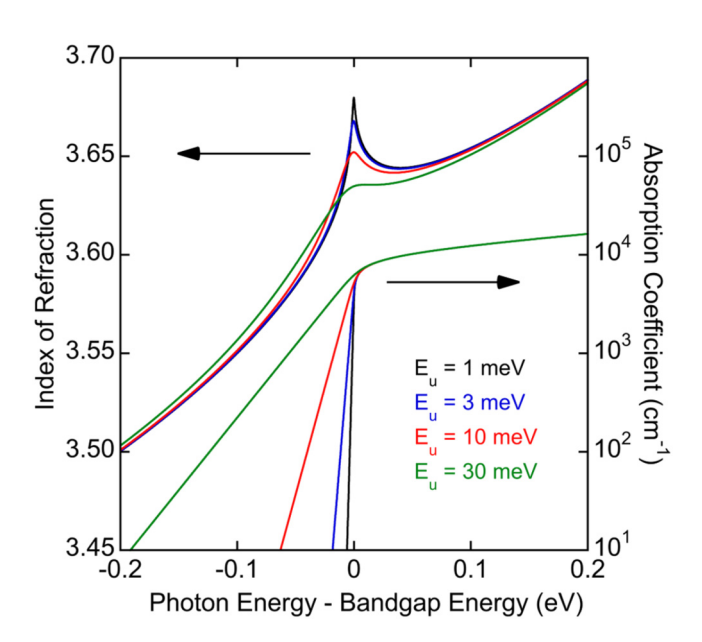


**FIG. 2.** Simulated index of refraction  $n(h\nu)$  (left vertical axis) and absorption coefficient  $\alpha(h\nu)$  (right vertical axis) in the vicinity of the absorption edge as a function of photon energy relative to the bandgap energy, with an Urbach energy of 1 meV (black), 3 meV (blue), 10 meV (red), and 30 meV (green). The simulated absorption edge model parameters are for the optical constants of GaAs.

[Eq. (10e)] is varied. This limits the optical constant change to that of the width of the absorption edge.

The shape of the peak in the index of refraction is sensitive to small changes in the Urbach energy. Due to Kramers-Kronig consistency, the width of the absorption edge is specified in the height and the width of the peak in the index of refraction. For small Urbach energies, the sharp absorption edge produces a sharp largeamplitude peak positioned at the bandgap. For large Urbach energies, the broad absorption edge produces a broad smaller-amplitude peak positioned slightly below the bandgap. One of the key elements of the absorption edge model [Eq. (10)] is that the value of the Urbach energy can be determined from either the index of refraction or the absorption coefficient, or both.

# **III. SAMPLE PROPERTIES AND STRUCTURAL CHARACTERIZATION**

The superlattice and bulk InAsSb samples investigated are grown by molecular beam epitaxy (MBE) on (100) n-type GaSb substrates using a Veeco Gen930 system. The sample structural cross sections are shown in Fig. 3 and consist of a  $2.5 \,\mu m$  thick and a 4.2 µm thick midwave InAs/InAsSb strain-balanced superlattice, a 2.5 µm thick and a 4.2 µm thick midwave InGaAs/InAsSb strainbalanced superlattice, a 5.0 µm thick longwave InAs/InAsSb strainbalanced superlattice, and a 4.2 µm thick midwave InAsSb bulk layer that is grown lattice-matched on the GaSb substrate without a buffer layer. The midwave superlattice samples are grown on a 110 nm thick lattice-matched InAsSb buffer layer and the longwave superlattice sample is grown on a 50 nm thick GaSb buffer layer.

Bare substrates

GaAs oxide GaSb oxide InAs oxide InSb oxide

Semi-insulating Undoped Undoped Undoped buffer layer. The midwave superlattice samples are grown on a

GaAs oxide	GaSb oxide	InAs oxide	InSb oxide	
Semi-insulating	Undoped	Undoped	Undoped	
GaAs	(p-type) GaSb	(n-type) InAs	(n-type) InSb	

#### MBE grown

InAs oxide	InAs oxide	InAs oxide	InAs oxide	
4.2 μm thick mid-wave bulk InAsSb	2.5, 4.2 μm thick mid-wave InAs/InAsSb superlattices	2.5, 4.2 μm thick mid-wave InGaAs/InAsSb superlattices	5.0 µm thick long-wave InAs/InAsSb superlattice	
	110 nm InAsSb	110 nm InAsSb	50 nm GaSb	
n-type GaSb substrate	n-type GaSb substrate	n-type GaSb substrate	n-type GaSb substrate	

FIG. 3. (Top row) Sample structure cross sections for semi-insulating GaAs and undoped GaSb, InAs, and InSb substrates. (Bottom row) Sample structure cross sections for molecular beam epitaxy grown (MBE) lattice-matched InAsSb, midwave strain-balanced InAs/InAsSb and InGaAs/InAsSb superlattices, and a longwave strain-balanced InAs/InAsSb superlattice. Bulk InAsSb is  $4.2\,\mu\mathrm{m}$  thick, the midwave InAs/InAsSb and InGaAs/InAsSb superlattices are 2.5 or  $4.2 \,\mu m$ thick, and the longwave InAs/InAsSb superlattice is  $5.0 \,\mu m$  thick.

**TABLE I.** Thickness, carrier type, and carrier concentration of the III-V substrates investigated.

Substrate	Туре	Thickness (µm)	Carrier concentration (cm <sup>-3</sup> )
GaAs	Semi-insulating	350	$8 \times 10^6$
GaSb	Undoped (p-type)	500	$1 \times 10^{17}$
InAs	Undoped (n-type)	500	$2 \times 10^{16}$
InSb	Undoped (n-type)	640	$2 \times 10^{14}$

All superlattice samples comprise a thin surface layer of native InAs oxide as the final period of each is terminated with a tensile InAs layer. The optical properties of the native oxide on the lattice-matched  $InAs_{0.911}Sb_{0.089}$  sample are assumed to approximate those of InAs oxide, as the  $\sim 9\%$  InSb oxide mole fraction is expected to be negligible in the analysis.

The optical constants of the binary constituents GaAs, GaSb, InAs, and InSb are investigated by performing spectroscopic ellipsometry measurements on commercially available (100) substrates. The GaAs substrate is semi-insulating and the GaSb, InAs, and InSb substrates are unintentionally doped. The substrates comprise a thin surface layer of native oxide that varies from one to several monolayers thick. Open for substrate thickness, carrier type, and carrier concentration are provided by the manufacturer and are listed in Table I. The sample cross sections are provided in Fig. 3, which also serve as the physical layer structure of the optical structure model used to calculate the ellipsometric angles  $\Psi$  and  $\Delta$ .

The bulk InAsSb and superlattice samples are investigated using high-resolution x-ray diffraction (XRD). Dynamical simulations are performed using X'Pert Epitaxy<sup>41</sup> to determine the tetragonal distortion and layer thicknesses. For bulk InAsSb, the tetragonal distortion is determined by adjusting the simulated Sb mole fraction to fit the measured diffraction pattern, while the layer thickness cannot be determined by x-ray diffraction due to the absence of Pendellösung fringes because the material is over  $4\mu$ m thick. For the superlattices, the period and tetragonal distortion are determined by fitting dynamical simulations to the experimental data, where the period is determined from the average separation between satellite peaks, and the tetragonal distortion is determined from the separation between the

substrate peak and the zero-order satellite peak. The method used to determine the superlattice tetragonal distortion and period thickness is described in a previous work. <sup>12</sup> The superlattice thickness is determined as the product of the best-fit period and the number of superlattice repeats from the growth record.

From the spectroscopic ellipsometry measurements, the thicknesses of the superlattices and bulk InAsSb are given by the best-fit of the optical structure model to the measured ellipsometric data. The superlattice period is given as the best-fit thickness divided by the number of repeats in the growth record. The growth details, tetragonal distortion, and thickness determined from both x-ray diffraction (XRD) and spectroscopic ellipsometry (SE) are provided in Table II. The midwave superlattice results reported are for a multi-sample fit that analyzes both the 2.5 and  $4.2\,\mu\mathrm{m}$  thick samples simultaneously. The GaSb buffer thickness in the longwave superlattice sample is determined from the growth record.

The layer thicknesses determined by ellipsometry are 0.6% to 3.1% greater than those determined from x-ray diffraction. Within the sensitivity of x-ray diffraction dynamical simulations, the  $4.2\,\mu\mathrm{m}$  thick InAsSb bulk layer and the longwave InAs/InAsSb superlattice display no tetragonal distortion as the main diffraction peak is coincident with the substrate peak. The midwave InAs/InAsSb and InGaAs/InAsSb superlattices exhibit small negative out-of-plane tetragonal distortion. Off-axis (511) high-resolution x-ray diffraction measurements from both InGaAs/InAsSb superlattices which contain significant out-of-plane distortion show no relaxation, indicating that these and the other samples are coherently strained.

# IV. SPECTROSCOPIC ELLIPSOMETRY MEASUREMENTS AND MODELING

The room temperature spectroscopic ellipsometry measurements are performed using J. A. Woollam IR-VASE and VASE ellipsometers that cover an energy range of  $0.032-1.00\,\mathrm{eV}$  ( $38.7-800\,\mathrm{eV}$ ) and  $0.5-6.5\,\mathrm{eV}$  ( $2.45-0.19\,\mu\mathrm{m}$ ), respectively. All measurements are performed near Brewster's angle using incident angles between 55° and 80° for each sample investigated. Brewster's angle is identified as the angle at which the p-polarized reflectivity,  $|R_p|^2$ , of the sample structure is the minimum that occurs between 74° and 77° for all wavelengths and all samples investigated. The substrate backsides are roughened to diffusely scatter backside

**TABLE II.** Bulk and superlattice material growth details, thickness, and tetragonal distortion. The layer and superlattice thicknesses are determined using x-ray diffraction (XRD) and spectroscopic ellipsometry (SE).

Wavelength Material		Thickness (µm)		Superlattice period (nm)		Superlattice	Tetragonal Distortion	Buffer thickness
	Material	XRD	SE	XRD	SE	repeats	(%)	(μm)
Mid-IR	InAsSb		4.23			•••	0.000	
	InAs/InAsSb	2.57	2.58	5.83	5.90	440	-0.043	0.108
		4.24	4.31	5.74	5.83	739	-0.030	0.105
	InGaAs/InAsSb	2.48	2.55	3.28	3.38	754	-0.280	0.108
		4.15	4.28	3.28	3.38	1267	-0.293	0.110
Long-IR	InAs/InAsSb	4.98	5.00	11.96	12.03	416	0.000	0.050

reflections at energies below the bandgap where the substrates are transparent. This greatly reduces the backside reflection of spurious depolarized light into the solid angle of detection.

The measurements are analyzed by constructing an optical structure model for each sample using Eqs. (2)-(7) and the sample cross sections in Fig. 3. The ellipsometric angles  $\Psi^{mod}$  and  $\Delta^{mod}$  are calculated using the optical structure model and fit to the measured ellipsometric angles  $\Psi^{exp}$  and  $\Delta^{exp}$ . During the fit, the known optical constants of all other layers are inputs to the model and the optical constants of the layer of interest are the best-fit parameters. In this analysis, two methods are used. In the first method, the optical constants at each measured photon energy are determined for each individual ellipsometric angle pair using the so-called "point-by-point" fit, 42 which assumes no particular spectral dependence of the optical constants. During this process, the optical constants are iteratively fit to each measured angle pair  $\Psi^{exp}$  and  $\Delta^{exp}$ , where layer thickness is not uniquely determined for the set of the individual measured angle pairs and thus must be ascertained by another means. In the second method, the optical constants are presumed to have the spectral dependence of the absorption edge model in Eq. (10) that is globally fit to the measured spectrum of angle pairs  $\Psi^{exp}$  and  $\Delta^{exp}$ , with layer thickness as a unique fit parameter. Using this method, it is possible to fit for the thickness of any or all other layers in the sample.

Accurately determining the surface oxide thickness in ellipsometric measurements is important and challenging as it strongly influences the magnitude of the extracted absorption coefficient of the underlying layer and typically cannot be distinguished from the best-fit optical constants of the underlying layer. This observation is understood as follows. Near Brewster's angle, the p-polarized Fresnel reflection coefficient is highly sensitive to changes in amplitude and phase compared to the s-polarized Fresnel reflection coefficient. As such, the presence of a transparent surface oxide induces a linear thickness-dependent phase shift that is large for ppolarized light and small for s-polarized light, resulting in a significant increase in the phase difference  $\Delta$  and hence in the imaginary part  $\sin(\Delta)$  of the phase term  $e^{i\Delta} = \cos(\Delta) + i\sin(\Delta)$ . On the other hand,  $tan(\Psi)$  and, hence, the real part  $tan(\Psi)cos(\Delta)$  is relatively insensitive to oxide thickness. Note that small changes in  $\Delta$  impact the optical constants to first order in the imaginary part and to second order in the real part.

The measured phase difference  $\Delta^{\text{exp}}$  of the entire structure includes contributions from both the oxide and underlying layers, which is straight forward to deconvolve when the thickness and optical constants of the oxide layer are known. The oxide layer thickness varies with both material and sample age as various oxides grow at different rates over time when exposed to the ambient. As such, the oxide thickness is generally not known and is difficult to estimate. Any error in the estimate of the oxide thickness results in a spurious phase difference that is assigned to the underlying layer, and that strongly affects the imaginary part of the extracted optical constants, with the real part weakly affected. As a result, spurious shifts in  $\Delta$  strongly affect the magnitude of the measured absorption coefficient, while the index of refraction is relatively unaffected.

For example, when the oxide thickness is underestimated, the magnitude of the extracted absorption coefficient of the underlying

layer is overestimated and vice versa. Misallocation of oxide thickness results in the addition of a spurious (positive or negative) background term to the absorption coefficient spectrum that is proportional to the phase thickness  $\beta$  that is proportional to the oxide index of refraction and inversely proportional to the wavelength. This negative wavelength power law distinguishes the spurious background absorption from the physical free-carrier sub-bandgap absorption that, for example, exhibits a positive wavelength power law on the order of 2 in GaAs, <sup>43</sup> GaSb, <sup>44</sup> InAs, <sup>45</sup> and InSb. <sup>46,47</sup> Another type of observed sub-bandgap absorption is that owing to the inter-band optical transitions in n-type GaAs <sup>43</sup> and GaSb <sup>44</sup> that exhibit a nearly constant background absorption below the bandgap.

The Jellison–Sales method for transparent glasses<sup>48</sup> is commonly used to evaluate oxide thickness,<sup>46</sup> which assumes that the underlying layer of interest is transparent at energies below the bandgap. This assumption is inherent in the optical constant absorption edge model [Eq. (10)] as the absorption coefficient decreases exponentially below the bandgap. When the underlying layer optical constants are fit with the absorption edge model, the native oxide thickness is a unique fit parameter in the optical structure model. The accuracy of the oxide thickness fit value depends on how transparent the material is below the bandgap. For the unintentional doping levels of the materials examined (see Table I), the sub-bandgap absorption <sup>43–47</sup> is less than 20 cm<sup>-1</sup> and negligible as it is below the sensitivity of the measurement.

The best-fit oxide thickness and substrate optical constants are determined for the binary materials as follows. The optical structure model consists of the ambient environment (0) above the native oxide layer (1) that is on top of the semi-infinite substrate material (2). An index of refraction  $N_0 \cong n \cong 1$  is used for the ambient. The native oxide optical constants are obtained from the literature and the substrate optical constants are determined as the best-fit results. Using an initial guess for the native oxide thickness and a semi-infinite substrate thickness, a point-by-point fit is performed to acquire the point-by-point optical constants of the substrate material. The oxide thickness is adjusted and this process is repeated until the point-by-point absorption coefficient is near zero below the onset of absorption at the band edge. The absorption edge model [Eq. (10)] is then fit to the point-by-point index of refraction and absorption coefficient by minimizing the objective function

$$\chi_{n\alpha}^2 = \sum_{j=1}^{J} \left[ \left( n_j^{\text{mod}} - n_j^{\text{pt}} \right)^2 + \left( \frac{hc}{4\pi h \nu} \right)^2 \left( \alpha_j^{\text{mod}} - \alpha_j^{\text{pt}} \right)^2 \right]. \quad (11)$$

Here, J is number of point-by-point data points; the subscript j refers to the summation index of the data point; and  $n_j^{\text{mod}}$ ,  $n_j^{\text{pt}}$ ,  $\alpha_j^{\text{mod}}$ , and  $\alpha_j^{\text{pt}}$  are the modeled and point-by-point index of refraction  $n_j$  and absorption coefficient  $\alpha_j$ , respectively. The best-fit parameters from this process provide an initial guess for the substrate optical constants in subsequent analysis.

Next, the absorption edge model parameters and oxide thickness are determined by fitting the ellipsometric parameters from the optical structure model to the measured data by minimizing the objective function

$$\chi_{\Psi\Delta}^{2} = \sum_{j=1}^{J} \sum_{i=1}^{I} \left[ \left( \frac{\sin\left(\Psi_{i,j}^{\text{mod}}\right) - \sin\left(\Psi_{i,j}^{\text{exp}}\right)}{\sin\left(\sigma_{\Psi,i,j}^{\text{exp}}\right)} \right)^{2} + \left( \frac{\sin\left(\Delta_{i,j}^{\text{mod}}\right) - \sin\left(\Delta_{i,j}^{\text{exp}}\right)}{\sin\left(\sigma_{\Delta,i,j}^{\text{exp}}\right)} \right)^{2} \right]. \tag{12}$$

Here, I is the total number of measured angles of incidence and *J* is number of measured data points at each angle of incidence. The modeled and measured ellipsometric angles are  $\Psi_{i,j}^{\text{mod}}$ ,  $\Delta_{i,j}^{\text{mod}}$ and  $\Psi_{i,j}^{exp}$ ,  $\Delta_{i,j}^{exp}$ , respectively, where the subscript *i* refers to the summation index of the angle of incidence and j refers to the summation index of the data point. The standard deviations in the measured ellipsometric angles are  $\sigma_{\Psi,i,j}^{\exp}$  and  $\sigma_{\Delta,i,j}^{\exp}$ . The measured range of the phase difference  $\Delta$  is limited to  $2\pi$  radians, which allows the possibility of discontinuities from angle phase-wrapping. As such, the sine of the ellipsometric angles is employed in the objective function to map the angles to a continuous function that avoids the discontinuities in the  $\Delta$  data, which improves fit stability and accelerates convergence. Once a best-fit oxide thickness is obtained, a point-by-point fit is performed to extract the final point-by-point optical constants.

The optical constants of the substrate and the InAsSb buffer layer (when present) must be accurately measured and input into the optical structure model in order to accurately determine the optical constants of the layer of interest. Therefore, separate samples of these materials are measured and analyzed using spectroscopic ellipsometry, x-ray diffraction, and the methods outlined above. These samples consist of (i) a bare n-type GaSb substrate similar to those used in the growths and (ii) a single InAsSb buffer layer grown on a similar n-type GaSb substrate. For the n-type GaSb substrate, an optical structure model is created that consists of a GaSb oxide layer and the n-type GaSb substrate. For the InAsSb buffer, an optical structure model is created that consists of an InAs oxide layer, the InAsSb buffer layer, and a n-type GaSb substrate. The buffer layer thickness is determined from the Pendellösung fringe spacing observed from x-ray diffraction measurements and is set to that value in the optical structure model.

For the epitaxially grown samples, the steps to obtain the best-fit thicknesses and optical constants of the layer of interest are as follows. The optical structure model consists of the ambient with index of refraction  $N_0 \cong n \cong 1$ , an InAs oxide layer, a bulk or superlattice layer, a buffer layer when present, and an n-type GaSb substrate. The buffer layer thicknesses used in the optical structure model are fixed at those listed in Table II. A point-by-point fit is performed to acquire the initial optical constants of the superlattice layer using an initial guess for the native oxide thickness, the superlattice layer thickness determined by x-ray diffraction in Table II, and a semi-infinite substrate thickness. In the case of bulk InAsSb, the initial layer thickness is obtained from the growth record. The oxide thickness is adjusted until the point-by-point absorption coefficient is near zero below the onset of absorption at the bandgap. An initial set of model fit parameters are obtained by fitting the absorption edge model [Eq. (10)] to the preliminary point-by-point index of refraction and absorption coefficient by minimizing the objective function in Eq. (11). These results are used as initial guesses for the bulk or superlattice layer optical constants in the optical structure model. The optical structure model parameters  $\Psi^{mod}$  and  $\Delta^{mod}$  are fit to the measured values  $\Psi^{\text{exp}}$  and  $\Delta^{\text{exp}}$  by minimizing the objective function in Eq. (12), with the absorption edge model and the oxide, and bulk or superlattice layer thicknesses, as fit parameters. Using the best-fit oxide thickness, a point-by-point fit is performed to extract the final point-by-point optical constants of the bulk or superlattice layer.

All modeling is performed in MATLAB<sup>50</sup> where each fit utilizes the Levenberg-Marquardt algorithm<sup>51,52</sup> to minimize the objective function. The absorption edge model robustly converges to a set of best-fit parameters that are within 0.5 meV for the bandgap energy, TO phonon energy, and Urbach energy, and within 1% for all other fit parameters, given any set of reasonable initial guesses. On the other hand, the point-by-point fit method is highly sensitive to the initial guess as there are many multiple local minima for each photon energy in the objective function. As such, the following method is used to acquire an initial guess at each photon energy through each photon energy in the order from the highest to the lowest. The optimal moving average window size that produces the overall best-fit to the measured data varies from sample to sample of within the range of 1-25, where 25 is the typical value.

Since the miniband structure of each superlattice comprises different optical properties than its constituent materials, each superlattice is treated as a single layer with a unique set of optical constants. The absorption depth is on the order of  $10 \,\mu m$  for the superlattice materials in the vicinity of the bandgap. The samples with thick layers exhibit spurious interference peaks at regular intervals in the point-by-point optical constants. These peaks are a result of interference within the thick bulk or superlattice layers, where the spacing between peaks depends on thickness.

An effective strategy to significantly reduce the prominence of the spurious interference peaks is the implementation of a multisample fit<sup>42</sup> that can be performed when multiple samples with the same material and different thicknesses are available. Multi-sample fits are performed on the 2.5 and 4.2 µm thick InAs/InAsSb superlattices and the 2.5 and 4.2 µm thick InGaAs/InAsSb superlattices. In the multi-sample fits, an optical structure model is constructed for the  $2.5\,\mu\mathrm{m}$  thick and  $4.2\,\mu\mathrm{m}$  thick superlattices, where the best-fit superlattice optical constants are shared among the two samples. The oxide and superlattice layer thicknesses for each sample are separate fit parameters in each respective optical structure model. The objective function in Eq. (12) is altered to include the modeled and measured ellipsometric angles of both samples in the summation. The multi-sample fit increases the reliability of the

absorption edge model fit and the best-fit absorption edge parameters. Furthermore, the multi-sample fit significantly reduces the prominence of spurious interference peaks in the point-by-point

### V. COMPUTATION OF OPTICAL CONSTANTS

The measured ellipsometric data in the form of  $sin(\Psi)$  and sin( $\Delta$ ) are shown in Fig. 4 as solid blue circles for the 2.5  $\mu$ m thick [(a) and (b)] and 4.2 µm thick [(c) and (d)] midwave InAs/InAsSb superlattices. The multi-sample fit results are shown as solid black circles for the point-by-point model and solid red curves for the absorption edge model. The angle of incidence is indicated for each data set. The multi-sample fits agree with the measured data over the full measured range for both thicknesses, indicating that the growths are reproducible and nearly identical except for thickness. The magnitude of the interference oscillations is largest in the transparent region below the bandgap (ground-state transition energy near 0.2 eV) where a larger portion of the incident light reflects from the bottom interface. The oscillation frequency in sin  $(\Psi)$  and  $\sin(\Delta)$  changes with thickness, indicating that it is accurately determined from the results.

The optical constants provided by both the individual and multi-sample fits to the midwave InAs/InAsSb and InGaAs/InAsSb superlattices are plotted in terms of the index of refraction and absorption coefficient in Fig. 5. The point-by-point results are displayed as solid blue circles and the absorption edge model results are displayed as solid red curves, with the index of refraction on the left vertical axis and the absorption coefficient on the right vertical axis. The individual fit results for the 2.5 and 4.2 µm thick superlattices are shown in plots (a) and (b) and (c) and (d), respectively. The multi-sample fit results are shown in plots (e) and (f). The superlattice results are initially fit individually and then combined in multi-sample fits. In each plot, the bandgap energy is indicated as a vertical dashed line and the index of refraction at the bandgap is listed as  $n_g$ . The best-fit bandgap energy  $E_g$ , bandgap absorption coefficient  $\alpha_g$ , Urbach energy  $E_u$ , and transverse optical phonon energy  $E_{TO}$  are provided in each plot and are summarized in Table III with the other best-fit parameters, including the oxide and superlattice thicknesses. The bandgap wavelength is reported as well. The InAs/InAsSb superlattice measurement range is 0.032-0.78 eV and the InGaAs/InAsSb superlattice measurement range is 0.032-1.00 eV. For photon energies above 0.80 eV, the measured depolarization exceeds 10% as the signal-to-noise decreases at high energies. As such, an upper bound of 0.80 eV is set for the fit range. The lower bound is set at the lowest measured photon energy of 0.032 eV. The multi-sample best-fit parameter values fall in between the individual fit values. Compared to the InAs/InAsSb superlattices, the InGaAs/InAsSb superlattices exhibit a larger absorption coefficient, although at a larger bandgap (240 vs 195 meV), and a significantly larger Urbach energy (31 vs 10 meV).

The point-by-point fit and absorption edge model fit to the raw ellipsometric data shown in Fig. 4 agree reasonably well with the measurements. However, the extracted point-by-point optical constants shown in Fig. 5 exhibit significant noise with periodic spikes that become increasingly larger below the bandgap. Although the point-by-point optical constants contain substantial noise, they provide a valuable means of assessment as to the actual spectra shape of the optical constants. In addition to bucking out the spurious noise peaks, the absorption edge model reproduces the general shape of the point-by-point results, thus validating its function form. Significantly, the absorption edge model encapsulates the belowbandgap Urbach tail slope and the above-bandgap power law dependence of the absorption coefficient and the characteristic shape of the index of refraction peak in the vicinity of the bandgap.

Analysis of the measurements of the  $5.0 \mu m$  thick longwave InAs/InAsSb superlattice is shown in Fig. 6 as solid black circles for the point-by-point fit and solid red curves for the absorption edge model fit. The out-of-plane miniband structure is calculated using a Kronig-Penney<sup>12,13,20</sup> model for which the bound transition energies are indicated with vertical dashed lines. The slope of the index of refraction and absorption coefficient changes at the onset of transitions at higher photon energies.<sup>20</sup> The most significant slope change occurs near 0.437 eV that corresponds to the second electron and second heavy-hole miniband (e2-hh2) transition. Therefore, an upper fit limit of 0.400 eV is chosen for the absorption edge model fit that results in a good agreement with the point-by-point data in that range. Additional model terms would be necessary to effectively cover the measured range shown. The point-by-point fit is performed over the full measured range of 0.032-0.800 eV. Unlike the shorter wavelength samples measured, the index of refraction at long wavelengths does not display the characteristic peak at the fundamental bandgap, as it is, instead, dominated by the nearby and much stronger optical phonon absorption peak at 25 meV that causes the index of refraction to rapidly decrease below the bandgap.

Analysis of the measurements from the  $4.2 \,\mu \text{m}$  thick bulk InAs<sub>0.911</sub>Sb<sub>0.089</sub> layer is shown in Fig. 7 as solid black circles for the point-by-point fit and solid red curves for the absorption edge model fit. The spurious noise spikes appear in the point-by-point of optical constants at nearly the same interval as for the  $4.2 \,\mu\mathrm{m}$  thick superlattice samples (see Fig. 5). The presence of periodic noise peaks in both bulk and superlattice layers indicates that the noise is interference based and depends on layer thickness rather than the interfaces within the superlattice layers. The interference peak noise is likely due to inconsistencies between the optical structure model and the actual grown structure, such as imperfect lateral uniformity.

The analysis of the measurements of the undoped III-V binary substrates GaAs, GaSb, InAs, and InSb is shown in Fig. 8 as solid black circles for the point-by-point fit and solid red curves for the absorption edge model fit. The longer wave IR-VASE (0.032-1.00 eV) measurements are used for smaller bandgap InAs and InSb, while both the IR-VASE and VASE (0.032-6.5 eV) measurements are stitched together at 0.6 eV for larger bandgap GaSb and GaAs. The lowest measured photon energy of 0.032 eV (39  $\mu$ m) is set as the lower bound for the point-by-point and absorption edge model fits. The upper bound of the fit range is 0.7 eV for InAs and InSb, as the measured depolarization significantly increases beyond this. The upper bounds of fit range for GaAs and GaSb are 1.65 and 1.0 eV, respectively, as at these energies, there is an onset of a slope change in the optical constants that is due to contributions from the higher energy  $E_1$  transition<sup>53</sup> corresponding to the L-point<sup>54</sup> that is not included in the absorption edge model. The point-by-point absorption coefficient is not displayed at energies below the absorption

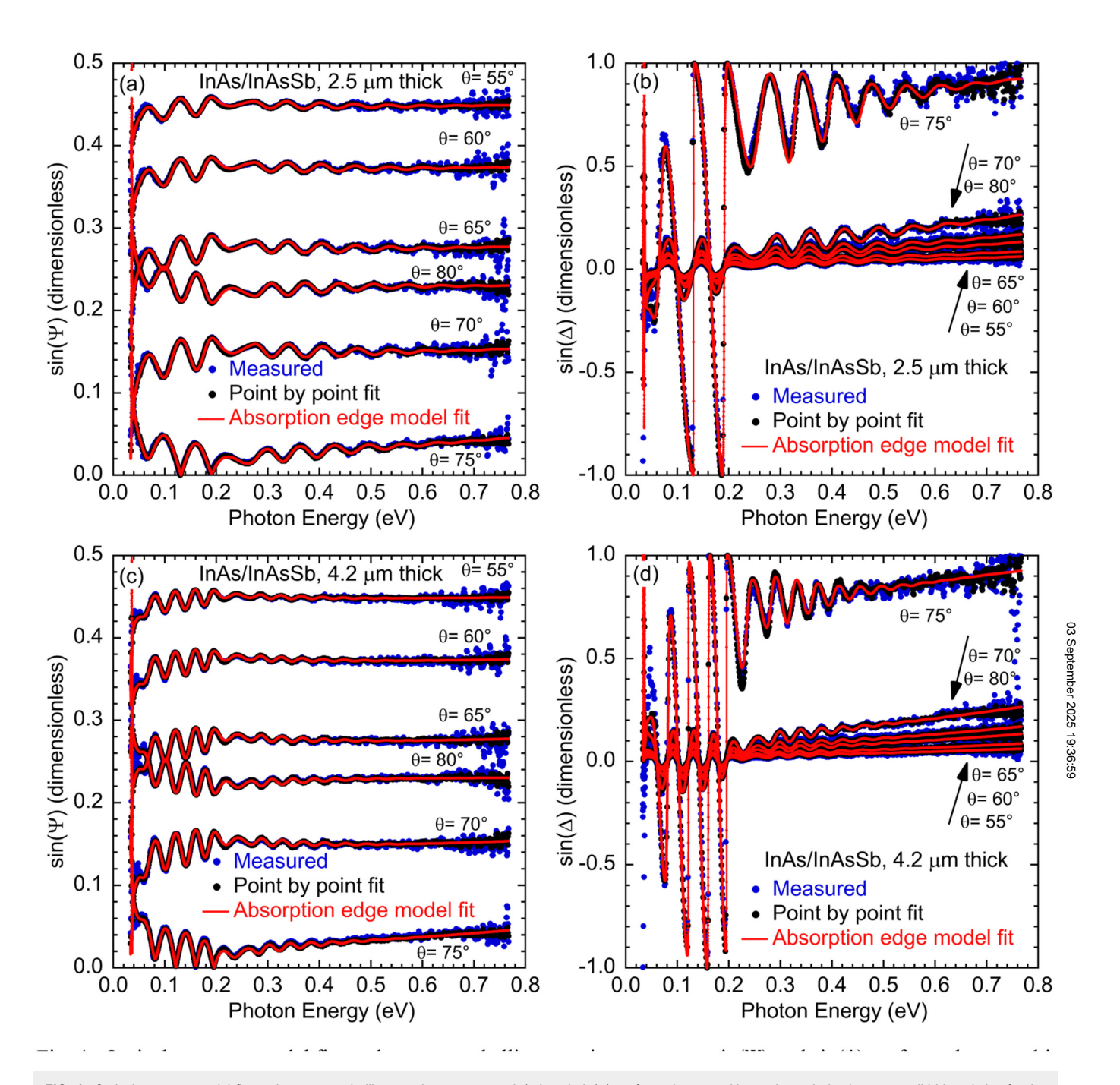


**FIG. 4.** Optical structure model fits to the measured ellipsometric parameters  $\sin(\Psi)$  and  $\sin(\Delta)$  performed as a multi-sample analysis shown as solid blue circles for the 2.5 [(a) and (b)] and  $4.2\,\mu\text{m}$  [(c) and (d)] thick lnAs/lnAsSb superlattices. The multi-sample point-by-point fit is shown as the solid black circles, and the multi-sample absorption edge model fit is shown as a solid red line. The angle of incidence is indicated for each data set.

edge, as it is predominantly noise because the absorption in this region is at or below the sensitivity of the instrument.

The magnitude of the absorption coefficient in the vicinity of the III-V binary bandgaps increases with bandgap energy.

The magnitude of the index of refraction in the vicinity of the bandgap is similar for antimonides (about 4.0 for InSb and GaSb) and similar for arsenides (about 3.6 for InAs and GaAs). On the other hand, the slope of the index of refraction of the indium-

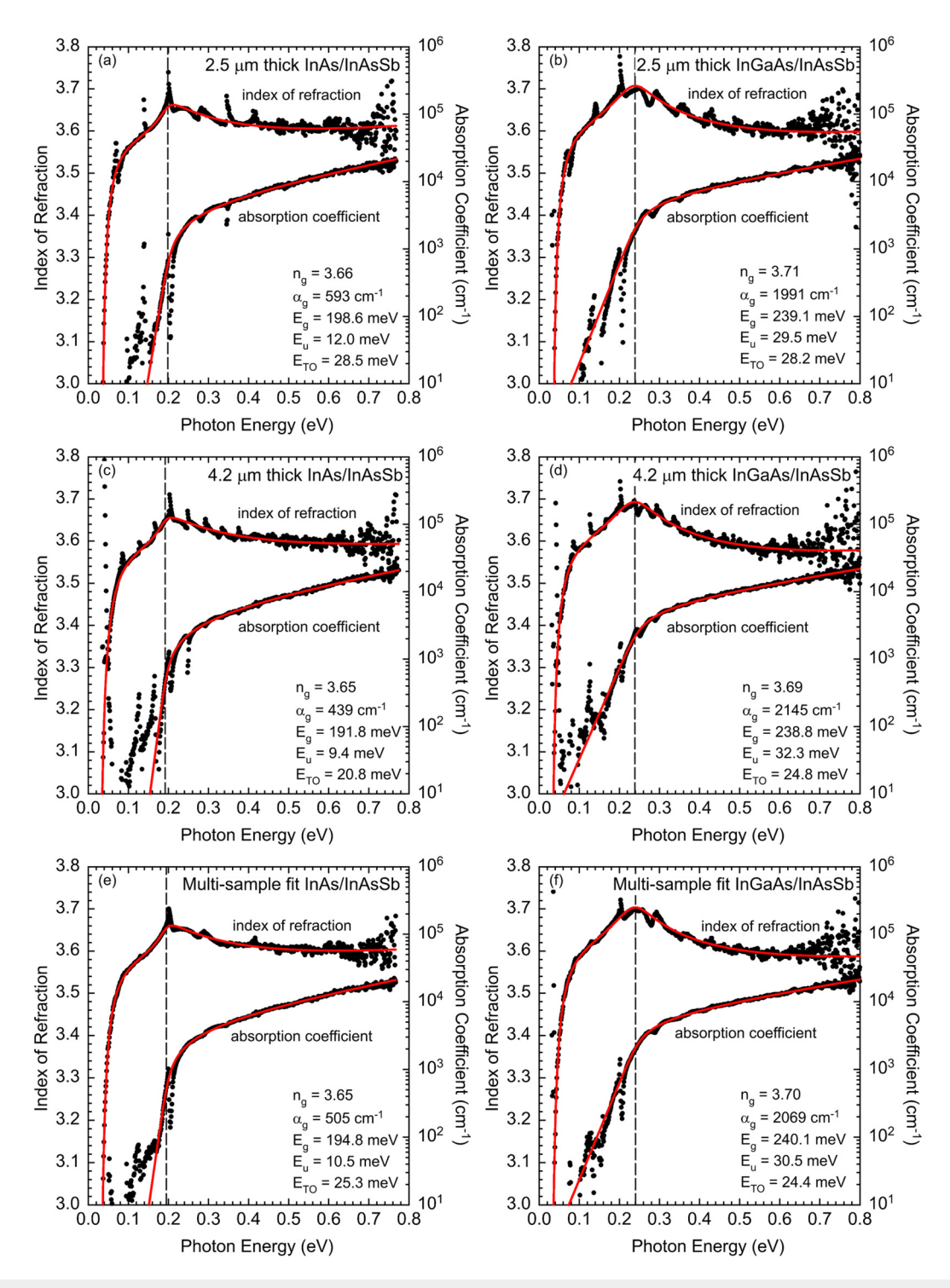


**FIG. 5.** Index of refraction and absorption coefficient determined using the point-by-point method are shown as filled black circles and the absorption edge model method is shown as a solid red line for the 2.5 μm thick [(a) and (b)], 4.2 μm thick [(c) and (d)], and multi-sample [(e) and (f)] InAs/InAsSb and InGaAs/InAsSb superlattice fits, respectively. The index of refraction and the absorption coefficient correspond to the left and right vertical axes, respectively. The best-fit bandgap energy, index of refraction, and absorption coefficient at the bandgap, Urbach energy, and TO phonon energy are provided. The bandgap energy is indicated as a vertical dashed line.

TABLE III. Best-fit parameters of the optical structure model to the ellipsometric data utilizing the absorption edge model for the 2.5 and 4.2 

mm thick InAs/InAsSb and InGaAs/InAsSb midwave superlattices. Both the individual and multi-sample fit results are provided. The best-fit superlattice and oxide thicknesses for each sample are slightly different for the multi-sample fits.

Superlattice type/material		Midwave In	As/InAsSb			Midwave InG	aAs/InAsSb	
Fit method	Individual		Multi-sample		Individual		Multi-sample	
Superlattice thickness (µm)	2.59	4.29	2.60	4.31	2.54	4.26	2.55	4.28
Oxide thickness (nm)	0.38	0.66	0.43	0.49	0.16	0.10	0.10	0.56
$\alpha_{\rm g}~({\rm cm}^{-1})$	593	439	505		1991	2144	2069	
$E_g$ (meV)	198.6	191.8	194.8		239.1	238.8	240.1	
$E_u$ (meV)	12.0	9.4	10.5		29.5	32.3	30.5	
$E_s$ (eV)	1.771	1.763	1.804		2.082	2.204	2.121	
$E_{\mathrm{TO}}$ (meV)	28.5	20.8	25.3		28.2	24.8	24.4	
$p_g$	0.555	0.599	0.5	582	0.375	0.378	0.369	
$a_m$	0.088	0.074	0.079		0.111	0.107	0.108	
$n_0$	3.082	3.135	3.094		3.055	3.000	3.062	
$n_1$	0.423	1.082	0.627		0.475	0.652	0.732	
Bandgap wavelength (μm)	6.24	6.46	6.	36	5.19	5.19	5.16	

containing binaries (InSb and InAs) are similarly flat whereas the gallium-containing binaries (GaSb and GaAs) exhibit a strong positive slope that is owed to the proximity of the higher energy  $E_1$ transition corresponding to the L-point<sup>54</sup> of 2.91 eV for GaAs<sup>5</sup>

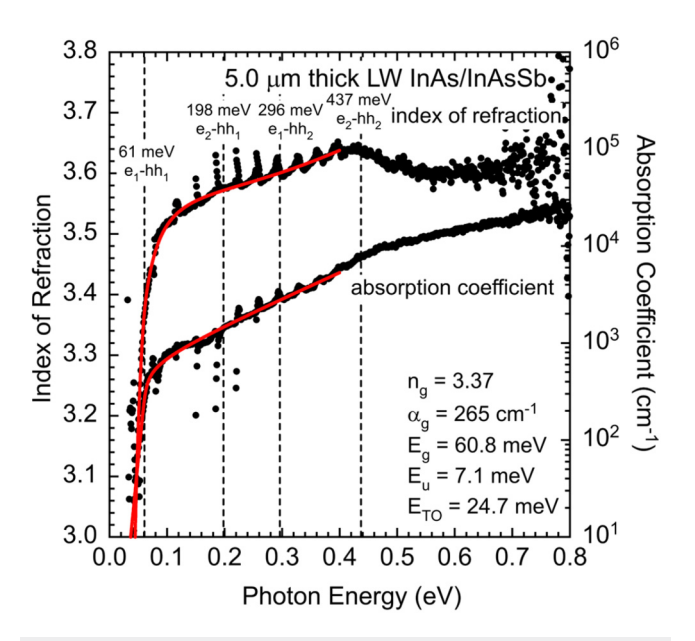


FIG. 6. Index of refraction and absorption coefficient of the longwave InAs/ InAsSb superlattice as determined by the point-by-point fit (solid black circles) and the absorption edge model fit (solid red curves). The index of refraction and absorption coefficient scales are on the left and right vertical axes, respectively. The best-fit bandgap energy, index of refraction, and absorption coefficient at the bandgap, Urbach energy, and transverse optical (TO) phonon energy are provided. The lowest energies of the bound miniband transitions are indicated as vertical dashed lines.

and 2.15 eV for GaSb,54 which results in a robust increase in absorption, 1.5 eV above the bandgap.

There is a slight offset in the measured phase difference  $\Delta$ where the IR-VASE and VASE measurements are joined, resulting in an offset in the point-by-point optical constants. The joined data sets are measured at the same angles of incidence; however, the two instruments may have small systematic offsets in the reported angle of incidence. Furthermore, the measurement location on the sample surface may differ between instruments, which could result in different oxide thicknesses as the native oxide layer typically in different oxide thicknesses as the native oxide layer typically fluctuates across the sample. 42,55 As described above, the phase difference  $\Delta$  is highly sensitive to oxide thickness.

# VI. MEASUREMENT AND MODELING ANALYSIS

The influence of the CO<sub>2</sub> absorption line on the InSb point-by-point absorption coefficient is observed at 290 meV  $(4.3 \,\mu\text{m})$ , where a 15% drop in the absorption coefficient occurs. Yet, the CO<sub>2</sub> absorption line is not observed in the index of refraction, indicating that the source of the disturbance is not Kramers-Kronig consistent. Analysis of the CO<sub>2</sub> absorption line shows that it can be removed from the absorption coefficient by assigning a double peak extinction coefficient with  $k_0 = 0.005$  at 289 meV and  $k_0 = 0.006$  at 292 meV to the ambient optical constants. This, however, causes a significant ± 0.4% disturbance in the index of refraction, indicating that the impact of CO2 absorption does not originate from such a large value of  $k_0$  for the ambient. Analysis that limits the disturbance in the index of refraction to the noise level places an upper limit on the ambient extinction coefficient of  $k_0 < 0.0004$  at the CO<sub>2</sub> absorption line.

The measurement signal is greatly reduced at the CO2 absorption line, resulting in a small 0.4% increase in depolarization and a small  $\pm 1^{\circ}$  disturbance in the phase difference  $\Delta$  for all angles of incidence. When the angle of incidence is greater than Brewster's angle, the phase difference  $\Delta$  decreases and vice versa. Similar to the oxide thickness analysis, this spurious change in  $\Delta$  is manifested

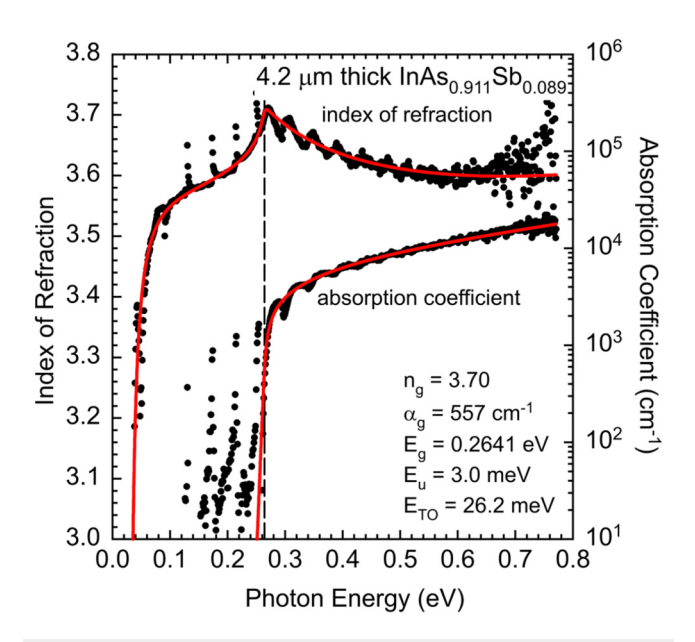


**FIG. 7.** Index of refraction and absorption coefficient for bulk InAs<sub>0.911</sub>Sb<sub>0.089</sub> as determined by the point-by-point fit (solid black circles) and the absorption edge model fit (solid red curves). The scales for the index of refraction and the absorption coefficient are provided on the left and right vertical axes, respectively. The best-fit bandgap energy, index of refraction, and absorption coefficient at the bandgap, Urbach energy, and TO phonon energy are provided. The bandgap energy is indicated as a vertical dashed line.

as an absorption notch at the  $CO_2$  absorption line. For the measurements at angles of incidence 68°, 72°, and 80° that are at least 4° from Brewster's angle, the phase difference  $\Delta$  is close to zero or 180° with  $\sin \Delta \leq 0.17$ . On the other hand, the measurements at 76° are close to Brewster's angle at 75.8° and the phase difference  $\Delta$  is close to 70°, with  $\sin \Delta \cong 0.94$  being significantly larger. The absorption coefficient extracted using only the 76° measurement does not exhibit a  $CO_2$  absorption notch, as the 1° disturbance in  $\Delta$  is small compared to 70°. Nevertheless, for the InSb results in Fig. 8, the significant decrease in the measured signal within the  $CO_2$  absorption notch results in a factor of 2 increase in the uncertainty of  $\Psi$  and  $\Delta$ , and a factor of 4 reduction in the fit weight.

The best-fit layer thicknesses and absorption edge model parameters for all samples examined are summarized in Table IV. The oxide thicknesses of the arsenides (GaAs and InAs) are smaller, at ~2 nm, compared to those of the antimonides (GaSb and InSb), at ~6 nm, and agree with values reported in the literature. 40 The oxide thicknesses of the epitaxially grown samples are notably thinner than those of the bare substrates, which is likely due to a shorter ambient exposure time for the grown samples.<sup>40</sup> The pub-GaSb,<sup>21,57</sup> InAs, 21,58 lished bandgap values of GaAs, 21,56 InSb<sup>21,46</sup> are comparable to the best-fit bandgap values. The binary substrate thicknesses are provided by the manufacturer.<sup>39</sup> The midwave InAs/InAsSb and InGaAs/InAsSb superlattice parameters are for multi-sample fits and, therefore, contain two oxide and two superlattice thicknesses. The bandgap wavelength is specified to show the position of each material on the infrared spectrum.

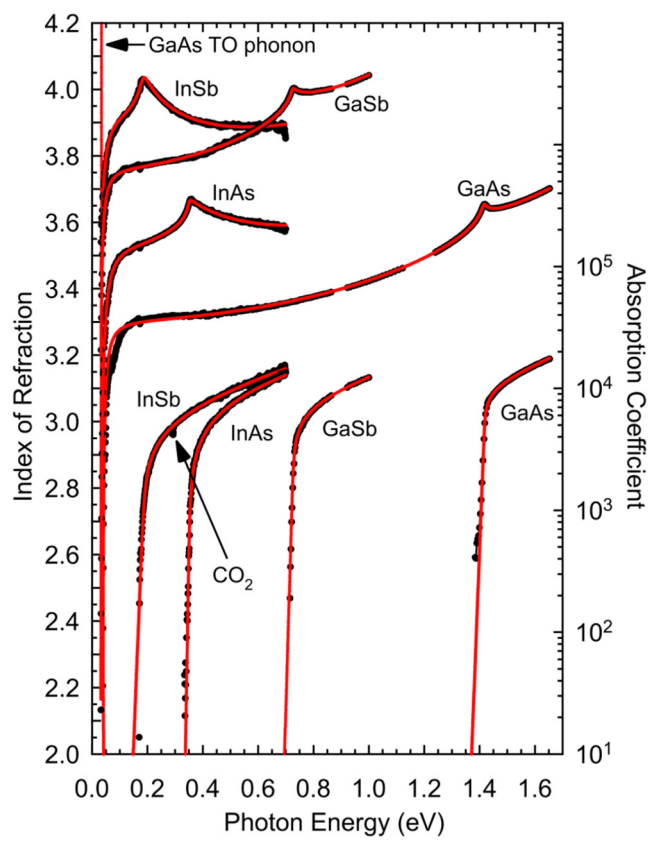


**FIG. 8.** Index of refraction and absorption coefficient for the III–V binary substrates GaAs, GaSb, InAs, and InSb as determined by the point-by-point fit (solid black circles) and the absorption edge model fit (solid red curves). The scales for the index of refraction and the absorption coefficient are on the left and right vertical axes, respectively. The impact of the CO<sub>2</sub> absorption line on the InSb absorption coefficient is indicated. The sharp dip and increase in the GaAs index of refraction due to the transverse optical (TO) phonon absorption peak is indicated at the upper left.

The oxide thicknesses are the best-fit results obtained by presuming that the materials are transparent below the absorption edge, which works well as the sub-bandgap absorption is below the sensitivity of the measurement. In the case where sub-bandgap absorption is not negligible, a more general solution is to note that any spurious misallocation of the oxide layer thickness, and hence phase difference  $\Delta$ , to the underlying layer results in a set of point-by-point optical constants that are not Kramers-Kronig consistent. This is straightforward to analyze using the Kramers-Kronig consistent absorption edge model. For example, a range of oxide thickness is estimated with a point-by-point fit performed at each oxide thickness. The absorption edge model is then independently fit to the point-by-point index of refraction and the point-by-point absorption coefficient, such that the absorption edge parameters, bandgap energy  $E_g$  and Urbach energy  $E_u$ , are independently determined for each. An absorption background

TABLE IV. Best-fit parameters of the optical structure model to the ellipsometric data utilizing the absorption edge model method for bulk and superlattice samples.

	Material system										
			Ві	ulk		Superlattices					
Material	GaAs	GaSb	InAs	$In As_{0.911} Sb_{0.089}$	InSb	Multi-samp InGaAs		Multi-sample midwave InAs/InAsSb		Longwave InAs/InAsSb	
Thickness (µm)	350	500	500	4.23	640	2.55	4.28	2.60	4.31	5.00	
Oxide thickness (nm)	1.78	7.92	2.09	1.43	4.50	0.10	0.56	0.43	0.49	0.12	
$\alpha_g  (\mathrm{cm}^{-1})$	4784	1851	587	557	870	20	69	50	)5	265	
$E_{g}(eV)$	1.4177	0.7257	0.3510	0.2641	0.1847	0.2401		0.1948		0.0608	
$E_u$ (meV)	7.7	5.7	3.2	3.0	7.8	30.5		10.5		7.1	
$E_s$ (eV)	4.35	5.81	6.44	3.56	4.97	2.12		1.80		1.01	
$E_{\mathrm{TO}}$ (meV)	33.8	27.3	26.8	26.2	23.2	24	.4	25	.3	24.7	
$p_g$	0.176	0.300	0.498	0.471	0.436	0.3	69	0.5	82	0.238	
$a_m$	0.481	0.161	0.048	0.053	0.039	0.1	08	0.0	79	0.072	
$n_0$	2.01	-1.15	0.33	2.41	1.19	3.0	06	3.0	)9	3.19	
$n_1$	0.38	0.22	0.53	0.49	0.46	0.7	73	0.0	53	1.44	
Bandgap wavelength (µm)	0.87	1.71	3.53	4.69	6.71	5.1	16	6.3	36	20.39	

term is added to the model to account for free-carrier absorption or spurious misallocated background absorption or both, such that there is no a priori assumption about transparency below the bandgap or the presence of spurious background absorption. The best-fit oxide thickness is the one that provides the closest values for the Urbach energy for both the index of refraction and the absorption coefficient, thus specifying Kramers-Kronig consistency.

This approach is tested on the binary substrate point-by-point data, noting that the absorption coefficient is significantly more sensitive to the misallocation of the phase difference  $\Delta$  and hence inaccuracies in oxide thickness. The Urbach energy as a function of oxide thickness rapidly shifts in the absorption coefficient analysis, with negative slopes of 17 meV/nm for GaAs and GaSb and 5 meV/nm for InAs and InSb, while it is nearly flat in the index of refraction analysis, with a positive slope of 0.8 meV/nm for GaAs and GaSb and a negative slope of 0.1 meV/nm for InAs and InSb, thus providing a convergence to a best-fit oxide thickness. In comparing to the best-fit values in Table IV, the values obtained with this method are 1.81 nm for GaAs, 7.78 nm for GaSb, 2.40 nm for InAs, and 4.2 nm for InSb, which are within 0.03 nm (2%) for GaAs, 0.14 nm (2%) for GaSb, 0.31 nm (15%) for InAs, and 0.27 nm (6%) for InSb, confirming the validity of the transparent assumption for the results in Table IV.

To quantify the sensitivity limit of the absorption measurements, covariance analysis<sup>59</sup> is performed to map the experimentally measured standard deviations in  $\Psi$  and  $\Delta$  into a standard deviation for the best-fit parameters. The standard deviations in  $\Psi$ and  $\Delta$  are determined from the standard deviations in the amplitude and phase of the measured sinusoidal ellipsometric signal recorded during multiple analyzer rotations.<sup>34</sup> The covariance analysis of the point-by-point optical constants, n and k, provide a respective uncertainty of 0.0004 and 0.0011 for GaAs, 0.0016 and 0.0016 for GaSb, 0.0056 and 0.0034 for InAs, and 0.0070 and 0.0041 for InSb. This corresponds to an uncertainty in the absorption coefficient measurement that is 160 cm<sup>-1</sup> (3.6%) for GaAs,

121 cm<sup>-1</sup> (5.8%) for GaSb, 122 cm<sup>-1</sup> (11.5%) for InAs, and 75 cm<sup>-1</sup> (7.2%) for InSb. The covariance analysis for the absorption edge model parameter  $\alpha_g$  that gives the absorption coefficient at the bandgap provides uncertainties of 74 cm<sup>-1</sup> (1.5%) for GaAs, 69 cm<sup>-1</sup> (3.7%) for GaSb, 34 cm<sup>-1</sup> (5.8%) for InAs, and 50 cm<sup>-</sup> (5.7%) for InSb. The covariance analysis of the grown samples shows a similar uncertainty in  $\alpha_g$  that ranges from 35 to 105 cm<sup>-1</sup>. These results indicate that the sensitivity of the measurement to the absorption coefficient is on the order of 100 cm<sup>-1</sup>, which is greater absorption coefficient is on the order of 100 cm<sup>-1</sup>, which is greater than the  $\alpha$  < 20 cm<sup>-1</sup> sub-bandgap absorption reported<sup>43-47</sup> for the  $\approx$ unintentional doping levels of the materials investigated.

The optical phonon absorption peak is observed within the  $\frac{\omega}{2}$ measurement range for GaAs. Therefore, in the analysis of GaAs, the Sellmeier oscillator in the absorption edge model [Eq. (10)] is replaced by a complex Lorentz oscillator.

$$N_{\text{TO}}(h\nu) = n_{\text{TO}}(h\nu) - ik_{\text{TO}}(h\nu)$$

$$= \frac{n_1}{1 - (h\nu/E_{\text{TO}})^2 - i\gamma h\nu/E_{\text{TO}}^2},$$
(13)

where  $N_{\rm TO}$  is the complex index of refraction for the transverse optical phonon and  $n_{\rm TO}$  and  $k_{\rm TO}$  are the real and imaginary parts, respectively. The revised oscillator includes an imaginary part that is fit to the TO phonon absorption peak in the GaAs absorption coefficient, where  $\gamma$  is the peak full-width at half-maximum. The Sellmeier oscillator is a specific case of a Lorentz oscillator with zero broadening that is used to describe the impact of the optical phonon on the index of refraction for the materials where the optical phonon absorption peak is outside of the measurement range.

The best-fit TO phonon energies determined in this work are listed in Table V and agree to within 1 meV to the published values for GaAs, 43,62,63 GaSb, 64 InAs, 63 InAsSb, 65 and InSb. 63 The TO phonon energy for the InAs/InAsSb and InGaAs/InAsSb

TABLE V. Transverse optical (TO) phonon energies for the bulk and superlattice materials investigated, determined as best-fit parameters of the absorption edge model. A Sellmeier oscillator is used when the measurement range does not include the TO phonon absorption peak. A Lorentz oscillator is used for GaAs because the measurement range includes the TO phonon absorption peak.

	Optical	phonon peak energy, E	Peak wid	th, γ (meV)	
	Sellmeier	Lorentz	Literature	Lorentz	Literature
GaAs		33.8	33.3 <sup>43,62,63</sup>	1.9	0.3 <sup>43,62</sup>
GaSb	27.5		26.66 <sup>64</sup>		
InAs	26.8		$26.95^{63}$		
InAs <sub>0.911</sub> Sb <sub>0.089</sub>	26.2		26.53 <sup>65</sup>		
InSb	23.2		$22.19^{63}$		
InGaAs/InAsSb	24.4				
MW InAs/InAsSb	25.3				
LW InAs/InAsSb	24.7	•••	•••		

superlattices are for the multi-sample analysis. The TO phonon energies of the superlattices lie between those of InAs and InSb. The low energy tail of the GaAs TO phonon absorption peak is not fully measured at the 0.032 eV cutoff of the measurement, resulting in an overestimation of  $\gamma$  compared to the literature value.

For the experimental results reported in this work, the number of significant figures specify an implied precision, where the last significant digit reported is on the order of the uncertainty determined by covariance analysis. For example, the uncertainty in the fit parameters obtained for the bandgap energy and the Urbach energy is on the order of 0.1 meV, with both parameters reported to a precision of 0.1 meV.

# VII. DISCUSSION

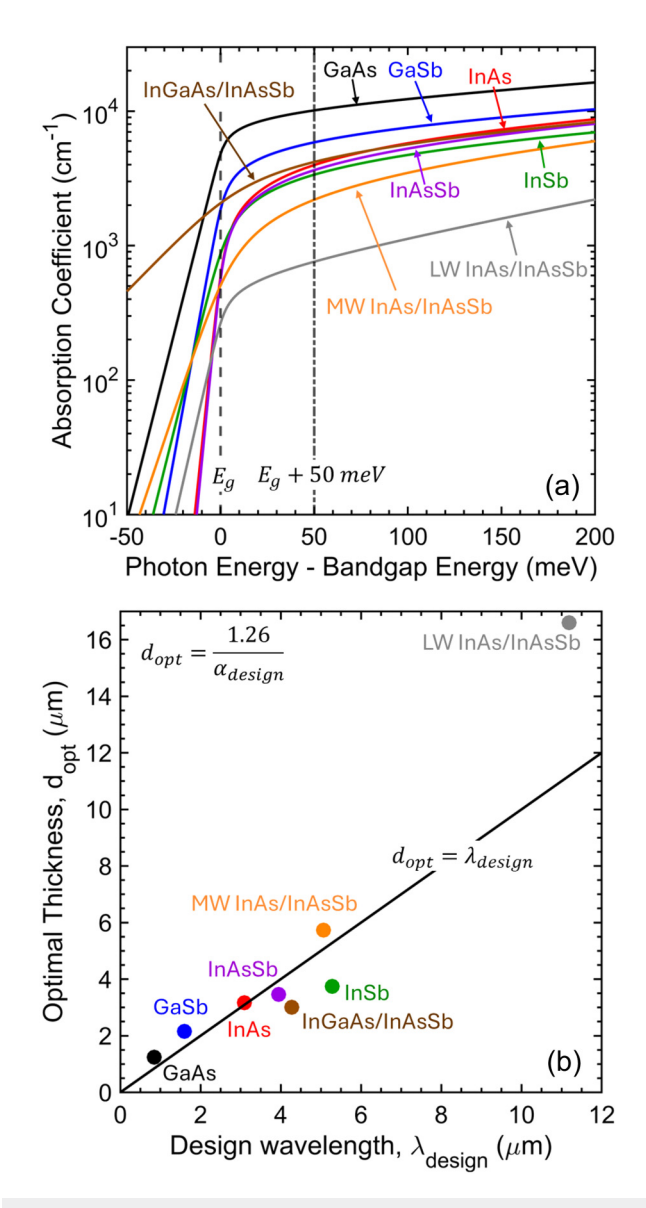
The absorption coefficients in the vicinity of the fundamental bandgap are compared in Fig. 9(a) for the bulk and superlattice materials examined. The multi-sample fit results are shown for the midwave superlattices. The results are plotted as a function of photon energy that is shifted so that the respective absorption edges coincide at their bandgaps; thus, the bandgap energy is indicated by a vertical dashed line at zero. For the purpose of photodetector thickness design, the absorption coefficient  $lpha_{
m design}$  is established at 50 meV above the bandgap, which is specified in the plot by the vertical dashed-dotted line. The optimal detector thickness, determined by the trade-off between photogenerated signal and parasitic generation recombination noise, is given as 600  $d_{\rm opt} = 1.26/\alpha_{\rm design}$  and is plotted in Fig. 9(b) as a function of the design wavelength  $\lambda_{design}$  specified at 50 meV above the bandgap. At this wavelength, the optical-absorption transitions are well into the continuum bands and away from the influence of band-tails. The unity slope line  $d_{\rm opt} = \lambda_{\rm design}$  is provided in the plot to illustrate photodetector absorption performance, where better performing materials lie below the line. The results indicate that optimal photodetector thickness is near the wavelength detected over a wide range of materials and bandgap energies. When cooled, the bandgap of these materials increases in energy, shifting the design wavelength toward shorter wavelengths with little change in the magnitude of the absorption, thus reducing the design wavelength while leaving the optimal thickness relatively unchanged.

The results in Fig. 9 show that the absorption transition strength of the materials examined decreases as the wavelength of detection increases, as indicated by the increase in optimal detector thickness that scales with wavelength. In the case of the bulk materials, this is due to a decrease in the conduction band electron density of states per unit energy as the bandgap shrinks, which is a result of the electron states separating in energy as the conduction band minimum stretches downward toward the valence band. In the case of the superlattices, the electron-hole wavefunction overlap decreases as the superlattice period increases as a means to reach smaller bandgaps by moving the electron miniband down toward the hole miniband.

A Kronig-Penney model is used to determine the out-of-plane are relatice band structure and electron and hole wavefunctions. superlattice band structure and electron and hole wavefunctions. Using the simulated wavefunctions, the square of the electron-hole wavefunction overlap at the ground-state transition energy is computed as 87.5% for midwave InGaAs/InAsSb, 64.2% for midwave of InAs/InAsSb, and 24.5% for longwave InAs/InAsSb. Wavefunction overlap decreases as the period increases due to increasing electron and hole localization. Therefore, longwave superlattices suffer from significantly reduced wavefunction overlap. 12,13 For the InAs/ InAsSb superlattices, the smaller wavefunction overlap is due, in part, to the asymmetric layer thicknesses required to obtain a strain-balance using tensile InAs.

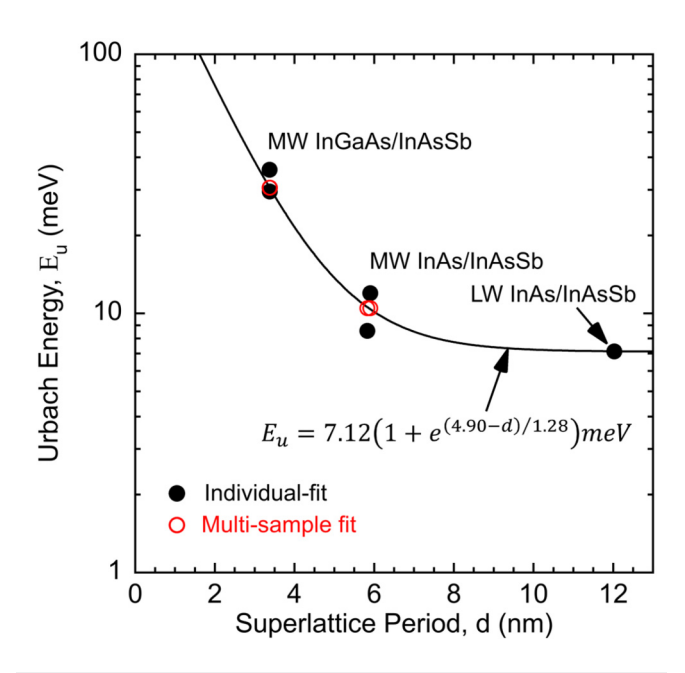
The introduction of Ga into InGaAs/InAsSb superlattices increases the tensile strain, allowing for more symmetric strain balancing. This reduces the period of the superlattice necessary to reach longer wavelengths, thereby increasing wavefunction overlap. The improved wavefunction overlap is observed in Fig. 9(b) where the optimal thickness for InGaAs/InAsSb is below the unity slope line and that of InAs/InAsSb is above. The unity slope line  $d_{\mathrm{opt}} = \lambda_{\mathrm{design}}$  is introduced as a means to compare absorption performance at different wavelengths, as shorter wavelength materials are naturally better absorbers.

In addition to absorption strength, the width of the absorption edge (Urbach energy) is another figure of merit for photodetectors, as it specifies the sharpness of the detector turn-on. The width of the absorption tail is a measure of disorder in the material that originates from both structural and thermal disorders. 17,67 In Fig. 9(a), bulk materials exhibit sharper absorption edges compared to superlattices. Since III-V materials are expected to display



**FIG. 9.** [Upper panel (a)] Absorption coefficient spectra (solid curves) as a function of energy relative to the bandgap for GaAs (black), GaSb (blue), InAs (red), InAs<sub>0.911</sub>Sb<sub>0.089</sub> (purple), InSb (green), midwave InAs/InAsSb superlattice (orange), midwave InGaAs/InAsSb superlattice (brown), and longwave InAs/InAsSb superlattice (gray). The bandgap for each material is indicated by a vertical dashed line at zero. The vertical dashed-dotted line specifies the material absorption coefficient at 50 meV above the bandgap. [Lower panel (b)] Optimal photodetector thickness for each material as determined by the absorption coefficient at the design wavelength specified at 50 meV above the bandgap.

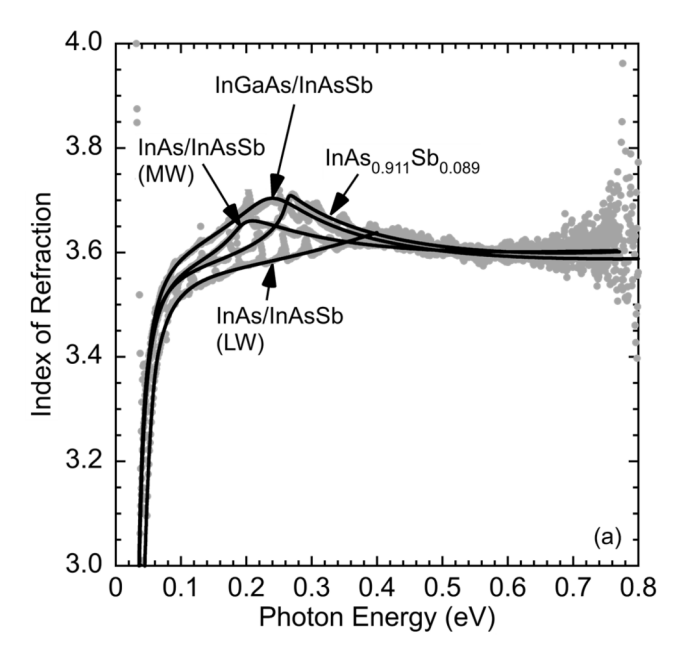
similar amounts of thermal disorder, the difference in tail width between bulk and superlattice materials is due to structural disorder. Different material systems contain different types of structural disorder that manifest mainly as point defects and ionized



**FIG. 10.** Urbach energy as a function of superlattice period thickness. The Urbach energy from the individual and multi-sample fits are shown as solid black circles and open red circles, respectively. As a guide to the eye, an exponential decay plus a constant offset is fit to the results and shown as a solid black curve. The equation with best-fit parameters is shown.

impurities in binaries, <sup>17</sup> compositional inhomogeneity in alloys, and compositional inhomogeneity at interfaces in superlattices. In addition to alloy disorder, superlattices exhibit chemical inhomogeneity at the interfaces that originates from the unintentional mixing of materials from adjacent layers that spans a few monolayers. 12 It is evident that the interface inhomogeneity takes up a larger percentage of the total disorder in superlattices with shorter periods. To illustrate this point, the Urbach energy is plotted as a function of superlattice period in Fig. 10. The results show that the Urbach energy is strongly dependent on period thickness, indicating that the presence of interfaces contribute significantly to the overall material disorder in superlattices. A constant term plus a power law term that is fit to the results indicates that the Urbach energy converges to 7.1 meV for large periods. In comparing the midwave superlattice optical properties, InGaAs/InAsSb offers improved absorption at the expense of a broader absorption edge.

The strain-balanced superlattices contain an average composition that is lattice-matched to GaSb<sup>12</sup> of either InAsSb (8.9% Sb) or GaInAsSb (8.8% Ga, 14.8%Sb). As such, the superlattices and bulk InAsSb are expected to share similarities in their optical constants. This is illustrated in Fig. 11, where the index of refraction [upper panel (a)] and the absorption coefficient [lower panel (b)] for bulk InAsSb, midwave InGaAs/InAsSb, midwave InAs/InAsSb, and longwave InAs/InAsSb are compared. The point-by-point results are specified as solid grey circles and the absorption edge model results are specified as solid black curves. The index of refraction and absorption coefficient of all materials converge at energies



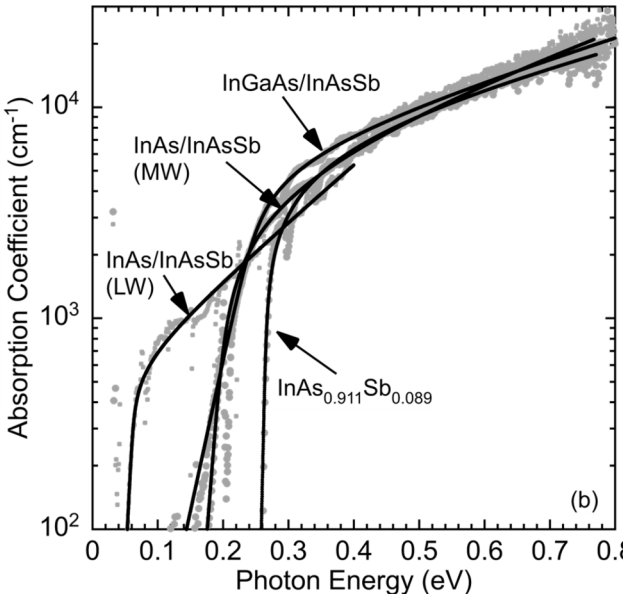


FIG. 11. Index of refraction plotted in upper panel (a) and absorption coefficient plotted in lower panel (b) for bulk InAs<sub>0.911</sub>Sb<sub>0.089</sub> midwave InGaAs/InAsSb, midwave (MW) InAs/InAsSb, and Iongwave (LW) InAs/InAsSb. Point-by-point fit is shown as solid gray circles and absorption edge model fit is shown as solid black curves

greater than 0.45 eV, a region where the optical transitions involve unbound electron and hole states that exhibit a bulk-like behavior based on the average composition of the superlattice material. The absorption coefficient of midwave InGaAs/InAsSb is slightly larger because of the Ga content. Kronig–Penney model simulations of

the out-of-plane miniband structure indicate that the onset of optical transitions between unbound states occur at energies greater than 0.4 eV for all superlattices. The results also demonstrate the role of bound miniband states in extending the optical-absorption cutoff to energies well below the bandgap of lattice-matched InAsSb. It is the structural design of the type-II superlattice period that controls the placement of bound states within the InAsSb bandgap that extend the absorption transitions to longer wavelengths. This occurs at cost to the electron-hole wave function overlap as shown by a decrease in the absorption coefficient as the absorption cutoff extends to lower energies.

# VIII. CONCLUSIONS

Strain-balanced type-II superlattices epitaxially grown on GaSb are investigated using spectroscopic ellipsometry and x-ray diffraction. The superlattices consist of midwave InGaAs/InAsSb, midwave InAs/InAsSb, and longwave InAs/InAsSb. For further evaluation and a more comprehensive understanding of the superlattice materials, the constituent ternary alloy InAs<sub>0.911</sub>Sb<sub>0.089</sub> and the constituent binaries GaAs, GaSb, InAs, and InSb are also investigated.

The optical constants of various materials are extracted from the ellipsometric measurements and expressed in terms of the index of refraction and the absorption coefficient that are subsequently examined in terms of photodetector performance. The results show that the optical-absorption transition strength of the materials examined decreases as the photodetection wavelength increases. As a result, it is observed that the optimal photodetector thickness is on the order of, and scales with, the photodetection wavelength over the wide range of material bandgap energies examined.

In assessing the midwave superlattice optical properties, compared to Ga-free InAs/InAsSb, the addition of Ga to InGaAs/ InAsSb offers enhanced absorption at the expense of a broader absorption edge. The introduction of Ga into the InGaAs/InAsSb superlattices increases the tensile strain, thus permitting symmetric strain balancing and shorter periods, thereby increasing wavefunction overlap. This, however, comes at the cost of greater structural disorder due to greater compositional inhomogeneity and a larger density of superlattice interfaces.

The strain-balanced superlattices contain an average composition that is lattice-matched to GaSb of either InAsSb (8.9% Sb) or GaInAsSb (8.8% Ga and 14.8%Sb). At energies greater than 0.45 eV the index of refraction and absorption coefficient of the superlattice materials converge to those of lattice-matched InAsSb. In this energy region, the optical transitions in the superlattice involve unbound electron and hole states that experience the average composition of the superlattice. Kronig–Penney model simulations of the out-of-plane miniband structure indicate that the onset of optical transitions between unbound states occur at energies greater than 0.4 eV for all superlattices.

At energies below the 0.264 eV bandgap of lattice-matched InAsSb, the structural design of the type-II superlattice period places bound miniband states within the InAsSb bandgap that extend the optical-absorption transitions to longer wavelengths. This occurs at a cost to the optical-absorption strength that is

proportional to the square of the electron–hole wavefunction overlap, which decreases from 87.5% for midwave InGaAs/InAsSb to 64.2% for midwave InAs/InAsSb to 24.5% for longwave InAs/InAsSb.

An optical constant model that yields equivalent numerical results to those given by a strict Kramers–Kronig consistent formulation is presented, which systematically describes the spectral shape of the index of refraction and absorption coefficient in the vicinity of the fundamental bandgap. In the model, the absorption coefficient is described in terms of an observed power law behavior at energies above the bandgap where continuum band to band optical transitions occur and an observed exponential Urbach absorption edge at energies below the bandgap where localized tail states participate in the band to band transitions. The model fit parameters provide physical insight into the absorption edge characteristics including the bandgap energy, Urbach energy, bandgap absorption coefficient, power law above bandgap, and optical phonon energy.

The spectral shape of the absorption edge in the vicinity of the bandgap produces a corresponding peak in the index of refraction via the Kramers–Kronig relation. This feature permits the analysis of the fundamental absorption edge without actually measuring the absorption coefficient. Thus, the absorption edge model facilitates the extraction of the absorption edge parameters from the index of refraction. This is particularly useful in extracting the Urbach energy that describes the impact of tail states on the absorption edge cutoff for photodetector applications.

In the analysis of the materials examined, the efficacy of the spectral shape of the absorption edge model is established by comparing it to a point-by-point model that does not assume any particular spectral shape of the optical constants. The superlattice and bulk InAsSb optical constants determined by the point-by-point fit contain spurious interference noise peaks. Multi-sample analysis greatly improves the point-by-point fit by reducing the prominence of the interference noise. On the other hand, the absorption edge model provides a smooth set of optical constants without spurious interference noise that are obtained directly from the ellipsometric data. The best-fit model parameters for the individual and multisample fits are consistent, indicating that the growths are reproducible. Covariance analysis of the absorption coefficient for both the point-by-point and absorption edge models indicates that the sensitivity limit of surface-reflection spectroscopic ellipsometry is on the order of 100 cm<sup>-1</sup>.

Analysis of the point-by-point optical constants of the layer of interest indicates that the index of refraction is relatively insensitive to inaccuracies in the oxide thickness compared to the absorption coefficient. As the oxide thickness increases, the phase shift of the p-polarized light increases, thereby changing the measured ellipsometric angle Δ, resulting in a decrease in the magnitude of the modeled absorption coefficient and a steeper Urbach tail. Thus, an inaccurate oxide thickness results in point-by-point fits that are not Kramers–Kronig consistent. As such, a method is presented that uniquely determines oxide thickness as the value that produces Kramers–Kronig consistent point-by-point optical constants. In practice, this is achieved by adjusting the oxide thickness until the absorption edge model fits independently to the point-by-point index of refraction and absorption coefficient, which results in a

similar set of best-fit parameters. The benefit of this approach is that it makes no assumption about transparency below the bandgap. The oxide thickness determined using this method agrees reasonably well with the best-fit oxide thickness determined from the optical structure model fits to the measured ellipsometric angles  $\Psi$  and  $\Delta$ , where the materials are assumed to be transparent directly below the bandgap absorption edge. The results from both methods are close enough to confirm that the samples are transparent directly below the bandgap.

# **ACKNOWLEDGMENTS**

The authors acknowledge financial support through research sponsored by the Air Force Research Laboratory<sup>68</sup> under Agreement No. FA9453-21-2-0047 and Section 219 Seedling for Disruptive Capabilities funding. The authors acknowledge use of facilities in the Eyring Materials Center at the Arizona State University. This work was also supported in part by the Air Force Office of Scientific Research under Award No. FA9550-24-1-0061, Air Force Research Laboratory under Award No. FA9453-23-2-0001, and National Science Foundation under Award No. DMR-2423992. Approved for public release: distribution is unlimited. AFMC PA No. 2025-3093.

#### **AUTHOR DECLARATIONS**

#### **Conflict of Interest**

The authors have no conflicts to disclose.

# **Author Contributions**

Marko S. Milosavljevic: Conceptualization (equal); Data curation (lead); Formal analysis (lead); Investigation (equal); Methodology (equal); Software (lead); Validation (equal); Visualization (equal); 🕏 Writing - original draft (lead); Writing - review & editing (equal). Rigo A. Carrasco: Conceptualization (supporting); Data curation (equal); Formal analysis (supporting); Investigation (supporting); Methodology (equal); Validation (supporting); Visualization (supporting). Alexander T. Newell: Conceptualization (supporting); Data curation (equal); Formal analysis (supporting); Investigation (supporting); Methodology (equal); Validation (supporting); Visualization (supporting). Jaden R. Love: Conceptualization (supporting); Data curation (equal); Formal analysis (supporting); Investigation (supporting); Methodology (equal); Validation (supporting); Visualization (supporting). Stefan **Zollner:** Conceptualization (supporting); Data curation (equal); Funding acquisition (equal); Investigation (supporting); Methodology (equal); Resources (equal); Supervision (equal); Validation (supporting); Writing - review & editing (supporting). Christian P. Morath: Conceptualization (supporting); Data curation (supporting); Formal analysis (supporting); Investigation (supporting); Methodology (equal); Validation (supporting); Visualization (supporting); Writing - review & editing (supporting). Diana Maestas: Conceptualization (supporting); Data curation (equal); Formal analysis (supporting); Investigation (supporting); Methodology (supporting); Validation (supporting); Visualization (supporting). Preston T. Webster: Conceptualization (supporting); Data curation (equal); Funding acquisition (equal); Methodology (equal);

Resources (equal); Supervision (equal); Validation (equal); Writing – review & editing (supporting). **Shane R. Johnson:** Conceptualization (equal); Formal analysis (equal); Funding acquisition (lead); Investigation (equal); Methodology (equal); Project administration (lead); Resources (equal); Supervision (lead); Validation (equal); Visualization (equal); Writing – original draft (equal); Writing – review & editing (lead).

#### DATA AVAILABILITY

The data that support the findings of this study are available within the article.

#### **REFERENCES**

- <sup>1</sup>C. Downs and T. E. Vandervelde, "Progress in infrared photodetectors since 2000," Sensors 13, 5054–5098 (2013).
- <sup>2</sup>D. Z. Ting, A. Soibel, A. Khoshakhlagh, S. A. Keo, S. B. Rafol, A. M. Fisher, B. J. Pepper, E. M. Luong, C. J. Hill, and S. D. Gunapala, "Advances in III–V semiconductor infrared absorbers and detectors," Infrared Phys. Technol. 97, 210–216 (2019).
- <sup>3</sup>J. Ai, M. Qin, M. Xue, C. Cao, J. Zhang, A. V. Kuklin, H. Wang, H. Zhang, Q. Zhang, H. Ågren, and L. Gao, "Recent advances of photodetection technology based on main group III–V semiconductors," Adv. Funct. Mater. 34, 2408858 (2019).
- <sup>4</sup>P. T. Webster, J. V. Logan, L. Helms, P. C. Grant, C. Hains, R. A. Carrasco, A. T. Newell, M. S. Milosavljevic, S. R. Johnson, G. Balakrishnan, D. Maestas, and C. P. Morath, "Demonstration of a 4.32 μm cutoff InAsSbBi nBn photodetector, a lattice-matched random alloy III–V solution for mid-wave infrared sensing," Appl. Phys. Lett. 123, 052101 (2023).
- <sup>5</sup>A. Rogalski, P. Martyniuk, M. Kopytko, P. Madejczyk, and S. Krishna, "InAsSb-based infrared photodetectors: Thirty years later on," Sensors 20, 7047 (2020).
- <sup>6</sup>P. Petluru, P. C. Grant, A. J. Muhowski, I. M. Obermeier, M. S. Milosavljevic, S. R. Johnson, D. Wasserman, E. H. Steenbergen, and P. T. Webster, "Minority carrier lifetime and photoluminescence of mid-wave infrared InAsSbBi," Appl. Phys. Lett. 117, 061103 (2020).
- <sup>7</sup>H. Estévez, A. Félix, M. Bergthold, O. Maksimov, H. B. Bhandari, C. P. Morath, A. W. Duchane, P. T. Webster, and D. Wasserman, "Enhanced minority carrier lifetime in bulk hydrogen-passivated InAsSbBi," Appl. Phys. Lett. **124**, 021104 (2024).
- <sup>8</sup>R. A. Carrasco, C. P. Morath, P. C. Grant, G. Ariyawansa, C. A. Stephenson, C. N. Kadlec, S. D. Hawkins, J. F. Klem, E. A. Shaner, E. H. Steenbergen, S. T. Schaefer, S. R. Johnson, and P. T. Webster, "Recombination rate analysis in long minority carrier lifetime midwave infrared InGaAs/InAsSb superlattices," J. Appl. Phys. 129, 184501 (2021).
- <sup>9</sup>B. V. Olson, E. A. Shaner, J. K. Kim, J. F. Klem, S. D. Hawkins, L. M. Murray, J. P. Prineas, M. E. Flatté, and T. F. Boggess, "Time-resolved optical measurements of minority carrier recombination in a mid-wave infrared InAsSb alloy and InAs/InAsSb superlattice," Appl. Phys. Lett. 101, 092109 (2012).
- <sup>10</sup>S. T. Schaefer, R. R. Kosireddy, P. T. Webster, and S. R. Johnson, "Molecular beam epitaxy growth and optical properties of InAsSbBi," J. Appl. Phys. 126, 083101 (2019).
- <sup>11</sup>R. R. Kosireddy; S, T. Schaefer; A, J. Shalindar, and S. R. Johnson, "Microstructure and surface morphology of InAsSbBi grown by molecular beam epitaxy," J. Appl. Phys. **126**, 095108 (2019).
- epitaxy," J. Appl. Phys. **126**, 095108 (2019).

  <sup>12</sup>M. S. Milosavljevic, P. T. Webster, and S. R. Johnson, "Impact of unintentional Sb in the tensile InAs layer of strain-balanced type-II InAs/InAsSb superlattices grown on GaSb by molecular beam epitaxy," J. Appl. Phys. **134**, 053103 (2023).

  <sup>13</sup>P. T. Webster, A. J. Shalindar, N. A. Riordan, C. Gogineni, H. Liang,
- <sup>13</sup>P. T. Webster, A. J. Shalindar, N. A. Riordan, C. Gogineni, H. Liang, A. R. Sharma, and S. R. Johnson, "Optical properties of InAsBi and optimal

- designs of lattice-matched and strain-balanced III-V semiconductor superlattices," J. Appl. Phys. 119, 225701 (2016).
- 14A. T. Newell, J. V. Logan, R. A. Carrasco, Z. M. Alsaad, C. P. Hains, J. M. Duran, G. Ariyawansa, G. Balakrishnan, D. Maestas, C. P. Morath, S. D. Hawkins, A. Hendrickson, and P. T. Webster, "Effects of doping and minority carrier lifetime on mid-wave infrared InGaAs/InAsSb superlattice nBn detector performance," Appl. Phys. Lett. 122, 171102 (2023).
- <sup>15</sup>G. Ariyawansa, C. J. Reyner, E. H. Steenbergen, J. M. Duran, J. D. Reding, J. E. Scheihing, H. R. Bourassa, B. L. Liang, and D. L. Huffaker, "Ingaas/InAsSb strained layer superlattices for mid-wave infrared detectors," Appl. Phys. Lett. 108, 022106 (2016).
- <sup>16</sup>C. H. Grein and S. John, "Temperature dependence of the Urbach optical absorption edge: A theory of multiple phonon absorption and emission sidebands," Phys. Rev. B 39, 1140 (1989).
- <sup>17</sup>S. R. Johnson, "Optical bandgap thermometry in molecular beam epitaxy," Ph.D. dissertation (University of British Columbia, 1995).
- <sup>18</sup>S. R. Johnson, T. Tiedje, and J. F. Young, "Temperature dependence of the Urbach edge in GaAs," J. Appl. Phys. 78, 5609–5613 (1995).
- <sup>19</sup>S. Imhof, A. Thränhardt, A. Chernikov, M. Koch, N. S. Köster, K. Kolata, S. Chatterjee, S. W. Koch, X. Lu, S. R. Johnson, D. A. Beaton, T. Tiedje, and O. Rubel, "Clustering effects in Ga(AsBi)," Appl. Phys. Lett. 96, 131115 (2010).
- <sup>20</sup>P. T. Webster, N. A. Riordan, S. Liu, E. H. Steenbergen, R. A. Synowicki, Y.-H. Zhang, and S. R. Johnson, "Absorption properties of type-II InAs/InAsSb superlattices measured by spectroscopic ellipsometry," Appl. Phys. Lett. 106, 061907 (2015).
- <sup>21</sup>S. T. Schaefer, S. Gao, P. T. Webster, R. R. Kosireddy, and S. R. Johnson, "Absorption edge characteristics of GaAs, GaSb, InAs, and InSb," J. Appl. Phys. 127, 165705 (2020).
- <sup>22</sup>P. P. Paskov, "Optical absorption and refraction spectra in highly excited GaSb," IEEE J. Quantum Electron. 30, 2771–2777 (1994).
- <sup>23</sup>R. J. Elliott, "Intensity of optical absorption by excitons," Phys. Rev. 108, 1384 (1957).
- <sup>24</sup>E. J. Johnson, "Absorption near the fundamental edge," in *Semiconductors and Semimetals*, edited by R. K. Willardson, and A. C. Beer (Elsevier, New York, 2967), Vol. 3, pp. 153–258.
- 25C. Tanguy, "Analytical expression of the complex dielectric function for the Hulthén potential," Phys. Rev. B **60**, 10660 (1999).
- 26F. Urbach, "The long-wavelength edge of photographic sensitivity and of the electronic absorption of solids," Phys. Rev. 92, 1324 (1953).
- <sup>27</sup>M. D. Sturge, "Optical absorption of gallium arsenide between 0.6 and 2.75 eV," Phys. Rev. 127, 768 (1962).
- <sup>28</sup>P. Y. Yu and M. Cardona, Fundamentals of Semiconductors Physics and Materials Properties, 4th ed. (Springer, Berlin, 2005), p. 279.
- <sup>29</sup>P. J. P. Tang, M. J. Pullin, and C. C. Phillips, "Binding energy of the free exciton in indium arsenide," Phys. Rev. B 55, 4376 (1997).
- <sup>30</sup>I. Pelant and J. Valenta, *Luminescence Spectroscopy of Semiconductors* (Oxford University Press, Oxford, 2016), p. 163.
- <sup>31</sup>C. Emminger, F. Abadizaman, N. S. Samarasingha, T. E. Tiwald, and S. Zollner, "Temperature dependent dielectric function and direct bandgap of Ge," J. Vac. Sci. Technol. B 38, 012202 (2020).
- 32S. Adachi, Properties of Group-IV, III-V and II-VI Semiconductors (John Wiley & Sons, Inc., Chichester, 2005), p. 251.
- $^{33}$ K. Johs and T. J. Jackson, "Development of a parametric optical constant model for  $Hg_{1-x}Cd_xTe$  for control of composition by spectroscopic ellipsometry during MBE growth," Thin Solid Films 313–314, 137–142 (1998).
- 34J. A. Woollam, Guide to Using WVASE: Spectroscopic Ellipsometry Data and Acquisition and Analysis Software (J. A. Woollam Company, 2018).
- <sup>35</sup>R. M. A. Azzam and N. M. Bashara, *Ellipsometry and Polarized Light* (North-Holland, New York, 1977).
- <sup>36</sup>F. Stern, "Dispersion of the index of refraction near the absorption edge of semiconductors," Phys. Rev. B 133, A1653 (1964).

- <sup>38</sup>J. D. Jackson, Classical Electrodynamics, 3rd ed. (Wiley, New York, 1999), pp. 333–334.
- $^{\mathbf{39}}$ Wafer Technology Company, 34 Maryland Road, Milton Keynes MK158HJ, UK.
- <sup>40</sup>Y. Mizokawa, O. Komoda, and S. Miyase, "Long-time air oxidation and oxidesubstrate reactions on GaSb, GaAs, and GaP at room temperature studied by x-ray photoelectron spectroscopy," Thin Sol. Films 156, 127–143 (1988).
- <sup>41</sup>PANalytical X'Pert Epitaxy, version 4.2, Almelo, The Netherlands.
- <sup>42</sup>T. N. Nunley, N. S. Fernando, N. Samarasingha, J. M. Moya, C. M. Nelson, A. A. Medina, and S. Zollner, "Optical constants of germanium and thermally grown germanium dioxide from 0.5 to 6.6 eV via a multisample ellipsometry investigation," J. Vac. Sci. Technol. B 34, 061205 (2016).
- <sup>43</sup>J. S. Blakemore, "Semiconducting and other major properties of gallium arsenide," J. Appl. Phys. 53, R123–R181 (1982).
- <sup>44</sup>A. Chandola, R. Pino, and P. S. Dutta, "Below bandgap optical absorption in tellurium-doped GaSb," Semicond. Sci. Technol. **20**, 886 (2005).
- <sup>45</sup>R. M. Culpepper and J. R. Dixon, "Free-carrier absorption in n-type indium arsenide," J. Opt. Soc. Am. 58, 96–102 (1968).
- <sup>46</sup>M. Rivero Arias, C. A. Armenta, C. Emminger, C. M. Zamarripa, N. S. Samarasingha, J. R. Love, S. Yadav, and S. Zollner, "Temperature dependence of the infrared dielectric function and the direct bandgap of InSb from 80 to 725 K," J. Vac. Sci. Technol. B 41, 022203 (2023).
- <sup>47</sup>. E. D. Palik, Handbook of Optical Constants of Solids, (Academic Press, Orlando 1985), p. 491.
- <sup>48</sup>G. E. Jellison and B. C. Sales, "Determination of the optical function of transparent glasses by using spectroscopic ellipsometry," Appl. Opt. **30**, 4310–4315 (1991).
- <sup>49</sup>S. Zollner, "Model dielectric functions for native oxides on compound semiconductors," Appl. Phys. Lett. **63**, 2523–2524 (1993).
- 50 MATLAB, version R2024a, The MathWorks, Inc., Natick, MA, USA (2024).
- <sup>51</sup>K. Levenberg, "A method for the solution of certain non-linear problems in least squares," Q. Appl. Math. 2, 164–168 (1944).
- <sup>52</sup>D. W. Marquardt, "An algorithm for least-squares estimation of nonlinear parameters," J. Soc. Ind. Appl. Math. 11, 431–441 (1963).
- parameters," J. Soc. Ind. Appl. Math. 11, 431–441 (1963). <sup>53</sup>D. E. Aspnes and A. A. Studna, "Dielectric functions and optical parameters of Si, Ge, GaP, GaAs, GaSb, InP, InAs, and InSb from 1.5 to 6.0 eV," Phys. Rev. B 27, 985 (1983).
- <sup>54</sup>J. R. Chelikowsky and M. L. Cohen, "Nonlocal pseudopotential calculations for the electronic structure of eleven diamond and zinc-blende semiconductors," Phys. Rev. B 14, 556 (1976).

- 55W. Yuan and D. C. Hall, "Variable-angle spectroscopic ellipsometry of InAlP native oxide dielectric layers for GaAs metal–oxide–semiconductor field effect transistor applications," J. Appl. Phys. 113, 103515 (2013).
- <sup>56</sup>D. D. Sell, H. C. Casey, and K. W. Wecht, "Concentration dependence of the refractive index for n- and p-type GaAs between 1.2 and 1.8 eV," J. Appl. Phys. 45, 2650–2657 (1974).
- 57 A. Joullié, A. Zein Eddin, and B. Girault, "Temperature dependence of the energy gap in gallium antimonide," Phys. Rev. B 23, 928 (1981).
- <sup>58</sup>J. R. Dixon and J. M. Ellis, "Optical properties of n-type indium arsenide in the fundamental absorption edge region," Phys. Rev. **123**, 1560 (1961).
- 59W. H. Press, S. A. Teukolsky, W. T. Vetterling, and B. P. Flannery, *Numerical Recipes in C* (Cambridge University Press, Cambridge, 1992).
- Recipes in C (Cambridge University Press, Cambridge, 1992).

  60S. L. Chuang, Physics of Photonic Devices, 2nd ed (John Wiley & Sons, Inc., Chichester, 2009), p. 190.
- <sup>61</sup>R. P. Feynman, R. B. Leighton, and M. Sands, *The Feynman Lectures on Physics* (Addison-Wesley, Reading, MA, 1964), Vol. I, Chap. 31, Sec. 2.
- 62S. Zollner, P. P. Paradis, F. Abadizaman, and N. S. Samarasingha, "Drude and Kukharskii mobility of doped semiconductors extracted from Fourier-transform infrared ellipsometry spectra," J. Vac. Sci. Technol. B 37, 012904 (2019).
- <sup>63</sup>D. J. Lockwood, G. Yu, and N. L. Rowell, "Optical phonon frequencies and damping in AlAs, GaP, GaAs, InP, InAs, and InSb studied by oblique incidence infrared spectroscopy," Solid State Commun. 136, 404–409 (2005).
- <sup>64</sup>S. S. Mitra, "Phonon assignments in ZnSe and GaSb and some regularities in the phonon frequencies of zincblende-type semiconductors," Phys. Rev. **132**, 986 (1963).
- $^{65}$ M. Erkuş and U. Serincan, "Phonon frequency variations in high quality  $InAs_{1-x}Sb_x$  epilayers grown on GaAs," Appl. Surf. Sci. 318, 28–31 (2014).
- <sup>66</sup>J. Piotrowski and W. Gawron, "Ultimate performance of infrared photodetectors and figure of merit of detector material," Infrared Phys. Technol. **38**, 63–68 (1997).
- 67G. D. Cody, T. Tiedje, B. Abeles, B. Brooks, and Y. Goldstein, "Disorder and the optical-absorption edge of hydrogenated amorphous silicon," Phys. Rev. Lett. 47, 1480 (1981).
- 68 The U.S. Government is authorized to reproduce and distribute reprints for Governmental purposes notwithstanding any copyright notation thereon. The views and conclusions contained herein are those of the authors and should not be interpreted as necessarily representing the official policies or endorsements, either expressed or implied, of Air Force Research Laboratory or the U.S. Government.